OXFORD

Human Molecular Genetics, 2023, Vol. 32, 15, 2485–2501
https://doi.org/10.1093/hmg/ddad075
Advance access publication date 12 May 2023
Original Article

A new mouse model of ATR-X syndrome carrying a common patient mutation exhibits neurological and morphological defects

Rebekah Tillotson[1,2,*], Keqin Yan[3], Julie Ruston[1], Taylor DeYoung[4], Alex Córdova[3], Valérie Turcotte-Cardin[3,5], Yohan Yee[4,6], Christine Taylor[1], Shagana Visuvanathan[1], Christian Babbs[2], Evgueni A. Ivakine[1,7], John G. Sled[4,6,8], Brian J. Nieman[4,6,8,9], David J. Picketts[3,5] and Monica J. Justice[1,10]

[1]Genetics and Genome Biology Program, The Hospital for Sick Children, The Peter Gilgan Centre for Research and Learning, Toronto, ON M5G 0A4, Canada
[2]MRC Molecular Haematology Unit, Weatherall Institute of Molecular Medicine, John Radcliffe Hospital/Headley Way, Oxford OX3 9DS, UK
[3]Regenerative Medicine Program, Ottawa Hospital Research Institute, Ottawa, ON K1H 8L6, Canada
[4]Mouse Imaging Centre, The Hospital for Sick Children, Toronto, ON M5T 3H7, Canada
[5]Cellular & Molecular Medicine, University of Ottawa, Ottawa, ON K1H 8M5, Canada
[6]Department of Medical Biophysics, University of Toronto, Toronto, ON M5G 1L7, Canada
[7]Department of Physiology, University of Toronto, Toronto, ON M5S 1A8, Canada
[8]Translational Medicine Program, The Hospital for Sick Children, The Peter Gilgan Centre for Research and Learning, Toronto, ON M5G 0A4, Canada
[9]Ontario Institute for Cancer Research, Toronto, ON M5G 0A3, Canada
[10]Department of Molecular Genetics, University of Toronto, Toronto, ON M5S 1A1, Canada

*To whom correspondence should be addressed. RT: MRC Molecular Haematology Unit, Weatherall Institute of Molecular Medicine, Oxford OX3 9DS, UK. Tel: +44 1865222398; Email: rebekah.tillotson@ndcls.ox.ac.uk

Abstract

ATRX is a chromatin remodelling ATPase that is involved in transcriptional regulation, DNA damage repair and heterochromatin maintenance. It has been widely studied for its role in ALT-positive cancers, but its role in neurological function remains elusive. Hypomorphic mutations in the X-linked ATRX gene cause a rare form of intellectual disability combined with alpha-thalassemia called ATR-X syndrome in hemizygous males. Clinical features also include facial dysmorphism, microcephaly, short stature, musculoskeletal defects and genital abnormalities. As complete deletion of ATRX in mice results in early embryonic lethality, the field has largely relied on conditional knockout models to assess the role of ATRX in multiple tissues. Given that null alleles are not found in patients, a more patient-relevant model was needed. Here, we have produced and characterized the first patient mutation knock-in model of ATR-X syndrome, carrying the most common causative mutation, R246C. This is one of a cluster of missense mutations located in the chromatin-binding domain and disrupts its function. The knock-in mice recapitulate several aspects of the patient disorder, including craniofacial defects, microcephaly, reduced body size and impaired neurological function. They provide a powerful model for understanding the molecular mechanisms underlying ATR-X syndrome and testing potential therapeutic strategies.

Introduction

ATRX (alpha-thalassemia/intellectual disability, X-linked) was initially identified as a trans-acting factor which when mutated downregulates alpha-globin expression. Such mutations are responsible for a rare condition in boys defined by the combination of alpha-thalassemia and intellectual disability (ATR-X syndrome) (1). To date, ATRX has been reported to have roles in heterochromatin maintenance, epigenetic patterning, transcriptional regulation and DNA damage repair (2). Since the discovery that ATRX is often lost in ALT-(alternative lengthening of telomeres) positive tumours (3), studies on the molecular mechanism by which ATRX suppresses the ALT pathway in cancer (4) far outnumber those on its roles in development.

ATR-X syndrome (Mendelian Inheritance in Man, 301040) is caused by hemizygous mutations in the X-linked *ATRX* gene in males. Mutations are often inherited from asymptomatic carrier females, who are protected by skewed X chromosome inactivation. All patients develop mild-severe intellectual disability, and 75% of patients have alpha-thalassemia with variable degrees of severity. The condition is also characterized by morphological features, including facial dysmorphism, microcephaly, short stature, hypotonia, kyphosis, scoliosis and genital abnormalities (5,6).

Global deletion of *Atrx* in mice results in early lethality at E9.5, due to trophectoderm defects (7). Therefore, the field has largely relied on conditional knock-out mice to investigate the role of ATRX in multiple tissues. Deletion of ATRX in the whole central nervous system or in the forebrain (by *Nestin-Cre* or *Foxg1-Cre*, respectively) results in postnatal lethality within 48 h of birth (8). Other models are viable into adulthood, with phenotypes revealing the importance of ATRX for the proper development and function of neurons (9,10), the retina (11,12), chondrocytes (13), skeletal muscle (14,15) and Sertoli cells (16). Additionally, an

Received: January 24, 2023. **Revised:** March 18, 2023. **Accepted:** May 5, 2023

analysis of *Atrx*$^{-/+}$ females found that preferential inactivation of the mutant allele is evolutionarily conserved (17).

The *ATRX* gene is composed of 35 exons, spanning ∼280 kb, and encodes a protein 2492 amino acids in length. Consistent with early embryonic lethality in knock-out mice, ATR-X patients carry hypomorphic alleles rather than complete loss of function mutations (such as large deletions). Several patients carry a nonsense mutation or frameshifting indel in early exons, which, at first glance, would be predicted to truncate large portions of the protein or deplete the transcript if targeted for nonsense-mediated decay (NMD). Instead, these "early truncating" mutations can be partially rescued by low levels of translation to produce protein lacking the extreme N-terminus from a downstream ATG, as demonstrated for R37X (18). An alternative rescue mechanism is splicing out mutated exons, converting a truncating mutation into a short in-frame deletion, again with low production levels (19). Notably, the resulting ATRX alleles with these "early truncating" mutations do not impact known functional domains. In contrast, missense mutations (and in-frame indels within exons that cause the gain/loss of up to 22 amino acids), cluster in two functional domains: the N-terminal chromatin binding ADD (ATRX-DNMT3-DNMT3L) domain and the C-terminal ATPase domain (20). Quantification of protein levels in EBV-transformed patient lymphocytes has helped determine the extent to which these mutations impact protein stability versus functionality. Protein levels in these mutants range from 7 to 51% of controls, and functional analysis of the more stable mutants has demonstrated reduced heterochromatin binding or chromatin remodelling activity (21–23).

A mouse line that carries a constitutive hypomorphic mutation should more effectively model ATR-X syndrome. Mice carrying a deletion of exon 2 model the "early truncating" mutations, expressing low levels of N-terminally truncated protein. These mice have been shown to recapitulate several aspects of the patient syndrome, including neurological defects and reduced brain size (24,25). Here, we produced the first model carrying a true ATR-X patient mutation. We chose the ADD mutant R246C (R245C in mice) because it is the most common patient mutation. As R246C protein has previously been shown to be relatively stable but have impaired binding to heterochromatin, we predicted that this model would shed light on the importance of the ADD domain (21,23). The mutant protein is sufficient to rescue the apoptotic cell loss phenotype that leads to death by 48 h, described in mice lacking ATRX in the forebrain (8,26). *Atrx*$^{R245C/y}$ mice survive to adulthood, developing several neurological defects and morphological features reminiscent of ATR-X syndrome, such as craniofacial dysmorphism, reduced body size and microcephaly. This represents the patient condition where microcephaly is acquired after birth (27). Intriguingly, the mutant protein is relatively stable (∼60% of controls) during embryonic development but declines dramatically to ∼10% of that seen in controls by 9 weeks of age, suggesting that instability may contribute more to the pathogenicity of R246C and other "stable" mutations than previously thought. We anticipate that the new *Atrx*$^{R245C/y}$ mouse model will be adopted by the field to expand our understanding of the molecular mechanisms underlying ATR-X syndrome and test future therapeutic avenues.

Results

Production of *Atrx*$^{R245C/y}$ knock-in mice

There are >250 patients with ATR-X syndrome and >100 causative mutations have been identified (19). Strikingly, the missense mutations and short in-frame indels fall almost entirely into two clusters located in the chromatin-binding ADD (ATRX-DNMT3-DNMT3L) domain and the ATPase domain (Fig. 1A), representing 43 and 32% of cases, respectively (Fig. 1B). A minority of mutations have occurred independently in more than one family, of which R246C is by far the most common and represents 18% of all cases (19,28). We therefore selected R246C as the most suitable candidate for a patient mutation mouse model of ATR-X syndrome. Knock-in mice were produced by electroporation of C57BL/6J zygotes with RNP (Cas9 protein and synthetic sgRNA) and a 142 nt donor template containing the desired mutation (c.733C>T; p.R245C, mouse homolog of R246C) and a silent PAM-abolishing mutation (c.729C>T; p.I243I) (Fig. 1C). We generated eight hemizygous male founders and one homozygous female founder carrying both mutations, and successfully bred five of the males. We established lines from two founders and carried out quality control assays on N1 heterozygous females and N2-3 males. Both lines carried the desired mutations (determined by Sanger sequencing), had no additional insertion of the donor template, and pups were born at the expected Mendelian ratio (Supplementary Material, Fig. S1). We chose line 1 for all future experiments. To best model ATR-X patients, hemizygous males were used for all analyses.

The R245C mutation impacts ATRX protein stability and binding to heterochromatin

Western blot analysis of ATRX protein levels in cortical tissue at birth (P0.5), found that the mutant protein was decreased to ∼60% of wild-type controls (Fig. 2A). This is consistent with a previous report that ATRX[R246C] is relatively stable (38% of controls) in patient lymphocytes (21). Surprisingly, repeating this analysis in mouse cortical tissue at 9 weeks of age found that the mutant protein was dramatically depleted to ∼10% of wild-type levels (Fig. 2B). This is unlikely to be a result of reduced *Atrx* transcription, as mRNA levels were only minorly decreased (∼80% of controls) at both timepoints (Fig. 2C). We therefore investigated protein stability with the translation-inhibiting drug, cycloheximide (CHX), in cultured cortical neurons derived from *Atrx*$^{R245C/y}$ and wild-type embryos. After 3 or 8 h of CHX treatment, the wild-type protein was present at similar levels as in DMSO-treated controls, but the mutant protein was depleted to 68 or 60% (Fig. 2D), indicating that the R245C mutation reduces stability. An analysis of adult spleen tissue found that ATRX[R245C] levels are similarly decreased to ∼15% of wild-type levels (Fig. 2E), demonstrating that the postnatal decrease in mutant ATRX levels was not unique to the brain. Functionality of the heterochromatin binding domain can be assessed in mouse cells and tissues by localization of ATRX at H3K9me3-rich pericentromeric foci (visualized as DAPI bright spots). Overexpression of human ATRX in cultured mouse fibroblasts revealed punctate staining for wild-type protein but diffuse staining for R246C protein (23). Here, we found that the R245C mutation impacts the recruitment of endogenous ATRX to heterochromatic foci, detected using immunofluorescence staining in mouse brain tissue at P0.5 (Fig. 2F). We conclude that impaired functionality is likely to be the main contributing factor to R245C pathogenicity during embryonic development, when ATRX[R245C] is relatively stable, but very low mutant protein levels resulting from reduced stability may be the dominating factor contributing to the pathogenicity of this mutation in adulthood.

Atrx$^{R245C/y}$ mice have reduced body size, brain weight and a craniofacial phenotype

The morphological features of ATR-X syndrome can be evident in children from a very early age and include short stature, postnatal

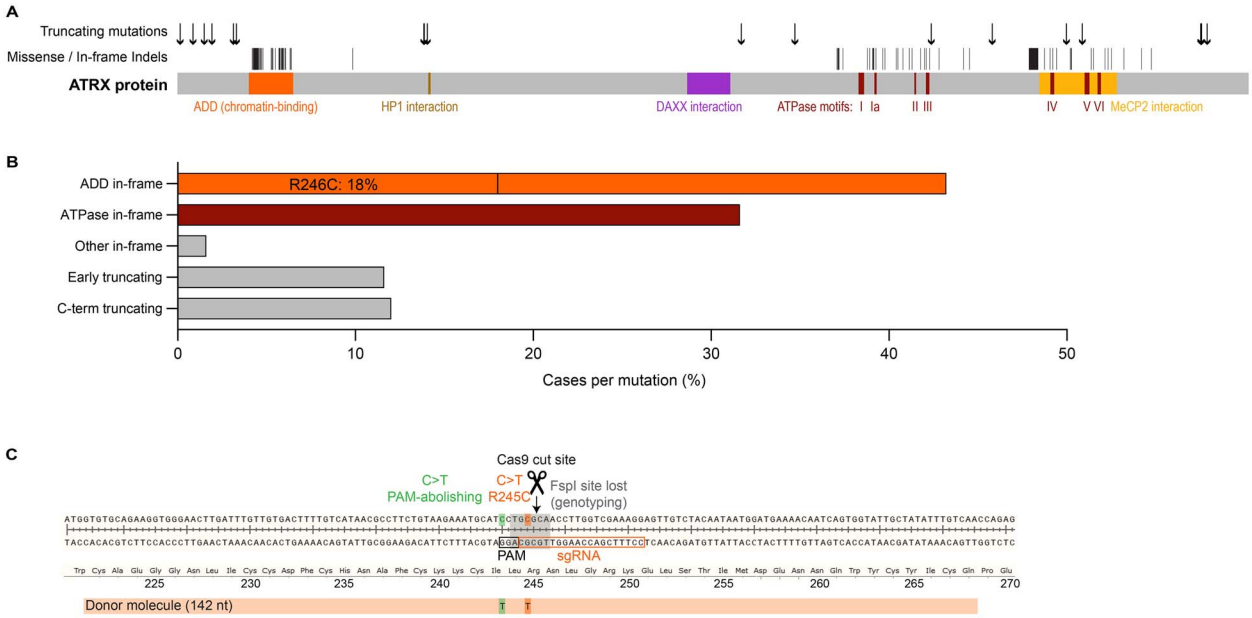

Figure 1. Production of *Atrx*$^{R245C/y}$ knock-in mice. (**A**) Schematic showing ATRX patient mutations, divided into truncating and in-frame mutations (missense and short indels). (**B**) Frequency of ATR-X syndrome-causing mutations identified in patients, separated by category (ADD in-frame, ATPase in-frame, other in-frame, "early truncating" and C-terminal truncating). (**C**) *Atrx*$^{R245C/y}$ mice were produced by Cas9-mediated editing in C57BL/6J embryos. Schematic of exon 9 of the mouse *Atrx* gene. A double-strand break was introduced by sgRNA-guided Cas9 and a 142 nt ss oligo containing the desired mutation (c.733C>T; p. R245C) and a PAM-abolishing silent mutation (c.729C>T; p. I243I) was incorporated. Mice were routinely genotyped using FspI digestion, which cleaves the WT PCR product.

microcephaly, facial dysmorphism, hypotonia and genital abnormalities (6). As such, we performed a variety of morphological analyses on the *Atrx*$^{R245C/y}$ mice to assess similarity to the human phenotype. *Atrx*$^{R245C/y}$ mice were lighter than wild-type littermate controls from weaning until at least 1 year of age (Fig. 3A). This was not due to a difference in the lean/fat ratio, measured by DEXA at P21 (Supplementary Material, Fig. S2A). X-ray analysis showed that mutant mice had smaller skeletons, with reduced body length in early (14 weeks) and late (52 weeks) adulthood (Fig. 3B). This is consistent with short stature in ATR-X syndrome (6). As patients have acquired microcephaly (27), we measured brain weight at 9 weeks, which was decreased in the mutants (Fig 3C). Facial dysmorphism is highly characteristic of ATR-X patients (6), so we assessed facial appearance in the mice (blind to genotype), observing that 11/19 (58%) of mutants in the initial cohort had visibly shortened snouts (Fig. 3D), compared with 2/20 (10%) of wild-type littermate controls. We quantified skull shape from X-ray images in two independent cohorts, aged 14 and 40 weeks. We saw a trend towards reduced cranial length that was significant only in the younger cohort (Fig. 3F). This was mirrored by a trend towards increased cranial index (cranial width/cranial length × 100) in both cohorts (Fig. 3G). More strikingly, mutant animals had a shorter zygomatic bone length (Fig. 3H), and the analysis of shape using "zygomatic index" (zygomatic width/zygomatic length ×100) confirmed this difference (Fig. 3I). This morphological change is reminiscent of the midface hypoplasia described in patients (20).

ATR-X patients have neonatal hypotonia (6), and mice lacking ATRX in skeletal muscle have reduced muscle mass and function at weaning, which is normalized by adulthood (14). In contrast, tibialis anterior (TA) muscle weight in *Atrx*$^{R245C/y}$ mice at P22 was proportional to the body weight (Supplementary Material, Fig. S2B). Similarly, grip strength, used as a measure of muscle strength, was also proportional to body weight in these animals (Supplementary Material, Fig. S2C). We assessed motor function more extensively in early adults (9–14 weeks of age) and found no differences in grip strength (Supplementary Material, Fig. S2C), minor differences in gait (Supplementary Material, Fig, S2D), but normal performance on the accelerating rotarod (Supplementary Material, Fig. S2E). As mice lacking ATRX in skeletal muscle show reduced performance with chronic exercise (15), we exercised an independent cohort of animals on a treadmill with an increasingly steep decline for four training days, followed by three trial days. Very few mice were unable to complete trials, which was comparable between genotypes (Supplementary Material, Fig. S2F). After chronic exercise, we saw no evidence of TA muscle damage from permeation of Evan's blue dye and no fibrosis in either genotype (Supplementary Material, Fig. S2G). Additionally, we observed no difference in the proportion of smaller muscle fibres in the mutants (Supplementary Material, Fig. S2H), a sign of muscle regeneration. The analysis of older adult mice also found no age-related decline in grip strength (Supplementary Material, Fig. S2C) and decreased stride length (Supplementary Material, Fig. S2I) is likely linked to smaller body size. Although 3/13 aged mutant mice failed to run on the treadmill used for gait analysis, an independent cohort displayed normal performance on the accelerating rotarod (Supplementary Material, Fig. S2J). Kyphosis is thought to be connected with muscle defects in patients since it was observed in muscle cKO mice (14). However, the kyphotic index was unaltered in *Atrx*$^{R245C/y}$ mice at weaning or in early/late adulthood (Supplementary Material, Fig. S2K). Overall, we were unable to detect muscle defects in *Atrx*$^{R245C/y}$ mice.

We did not observe any morphological differences in genitalia in our *Atrx*$^{R245C/y}$ mice and at least five hemizygous male founders and all tested males from both line 1 ($n = 3$) and line 2 ($n = 3$) were fertile. Although genital abnormalities are frequently reported in ATR-X syndrome patients (70–80%), they are most severe in those with C-terminal mutations (5,19). Reduced expression of

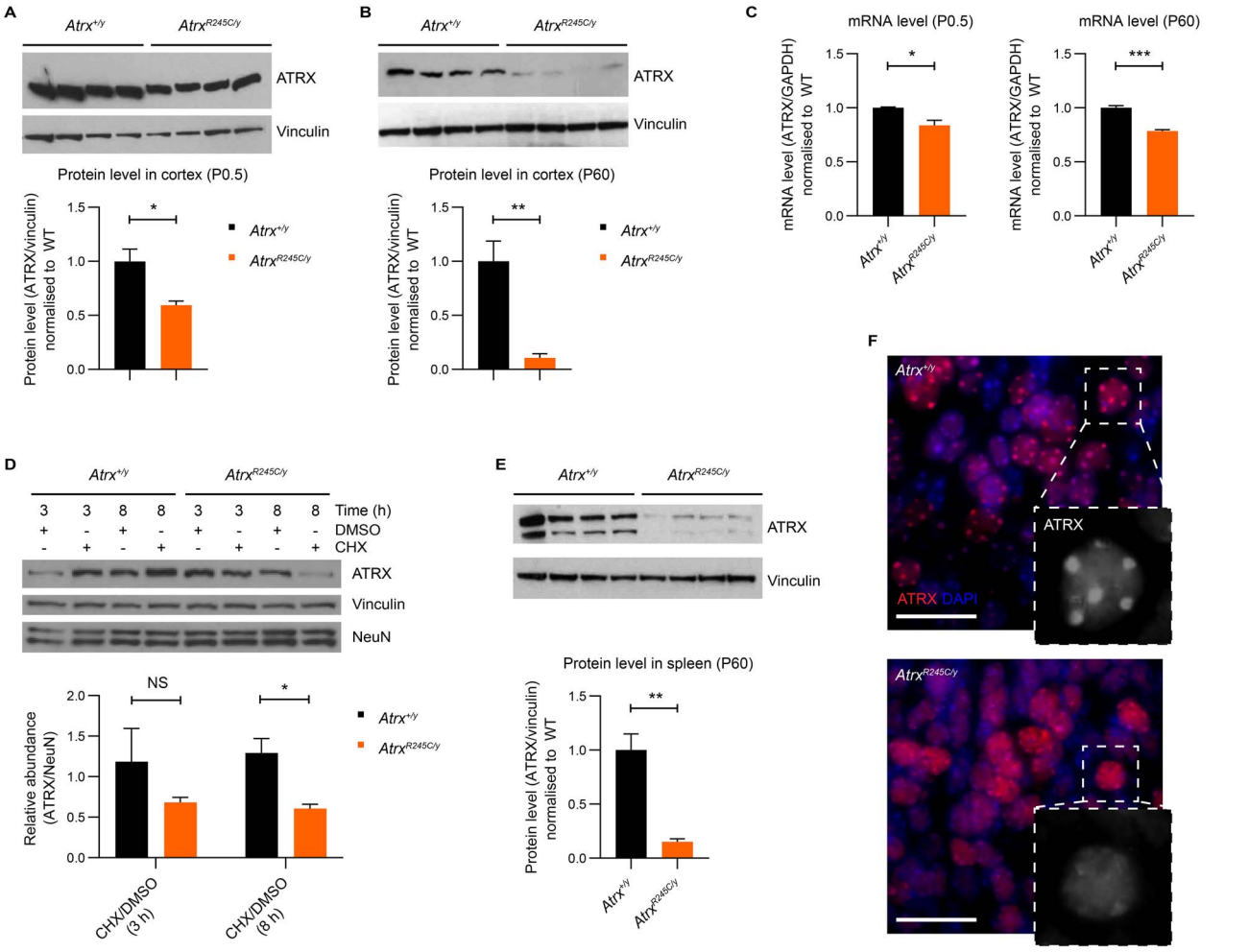

Figure 2. The R245C mutation impacts ATRX protein stability and binding to heterochromatin. (**A**, **B**) Western blot analysis of ATRX[R245C] protein levels in cortex of $Atrx^{R245C/y}$ males at (A) P0.5 and (B) P60, compared with wild-type controls ($n = 4$ per genotype for each). Quantification (below): R245C protein is present at 59.5% and 10.7% of normal levels at P0.5 and P60, respectively. Graphs show mean ± S.E.M. and genotypes were compared using *t*-tests: P0.5 $^{*}P = 0.014$; P60 $^{**}P = 0.004$. (**C**) qPCR analysis of *Atrx[R245C]* transcript levels in cortex at P0.5 (left) and P60 (right), compared with wild-type controls ($n = 3$ per genotype for each). mRNA is expressed at 83.8% and 78.4% of WT levels at P0.5 and P60, respectively. Genotypes were compared using *t*-tests: P0.5 $^{*}P = 0.03$; P60 $^{***}P = 0.0009$. (**D**) Cortical neurons at DIV7 derived from $Atrx^{+/y}$ and $Atrx^{R245C/y}$ E17.5 embryos were treated with DMSO vehicle or 100 μM Cycloheximide (CHX) for 3 or 8 h. Quantification (below) of the relative levels of ATRX (normalized to NeuN) in cells treated with CHX versus DMSO (three replicates). Graph shows mean ± S.E.M. and genotypes were compared using *t*-tests: 3 h $P > 0.5$; 8 h $^{*}P = 0.02$. (**E**) Western blot analysis of ATRX[R245C] protein levels in spleen at P60, compared with wild-type controls ($n = 4$ per genotype). Quantification (below): R245C is present at 15.2% of normal levels. Graph shows mean ± S.E.M. and genotypes were compared using a *t*-test: $^{**}P = 0.0014$. (**F**) Immunofluorescence staining of ATRX (red) in the cortex at P0.5. Nuclei are stained with DAPI (blue). Scale bar: 20 μm. Insert: 5× magnification of an example nucleus showing ATRX staining only (white).

alpha-globin (*HBA*), resulting in alpha-thalassemia, is detected in ~75% of ATR-X patients (5). Reduction in *HBA* expression, and therefore severity of alpha-thalassemia, correlates with the length of a G-rich VNTR repeat within the nearby HBAZ(ps) pseudogene (29). Analysis of the mouse *Hba* locus revealed that this repeat is not conserved across species (Supplementary Material, Fig. S3A). Accordingly, *Hba* expression and haematology are unaffected in $Atrx^{R245C/y}$ mice (Supplementary Material, Fig. S3B–G). Altogether, the $Atrx^{R245C/y}$ mice recapitulate several morphological features of ATR-X syndrome, including short stature, postnatal microcephaly and facial dysmorphism, but this model lacks hypotonia, genital abnormalities and alpha-thalassemia.

$Atrx^{R245C/y}$ mice display neurobehavioural phenotypes

As patients with ATR-X syndrome have mild to profound intellectual disability, we performed neurological tests on the $Atrx^{R245C/y}$ mice. Behavioural assays are typically done using young adults (9–14 weeks), when ATRX[R245C] protein levels were decreased to ~10% in the brain (Fig. 2B). All reflexes were normal based on SHIRPA analysis, but $Atrx^{R245C/y}$ mice had lower spontaneous activity than wild-type littermate controls (Fig. 4A). The Open Field test, which measures activity for a longer period of time, however, found normal exploratory behaviour (Supplementary Material, Fig. S4A). Mutants also displayed normal levels of anxiety with regards to open space (Supplementary Material, Fig. S4B), light (Supplementary Material, Fig. S4C) and height (Supplementary Material, Fig. S4D). These findings allowed us to assess more complex behaviours, without the compounding effects of altered activity or anxiety. We saw no genotypic differences in motor learning over three days of testing on the accelerating rotarod, with both genotypes displaying daily improvement (Supplementary Material, Fig. S4E). Spatial memory was assessed over four days in the Barnes Maze, where wild-type mice locate the hidden

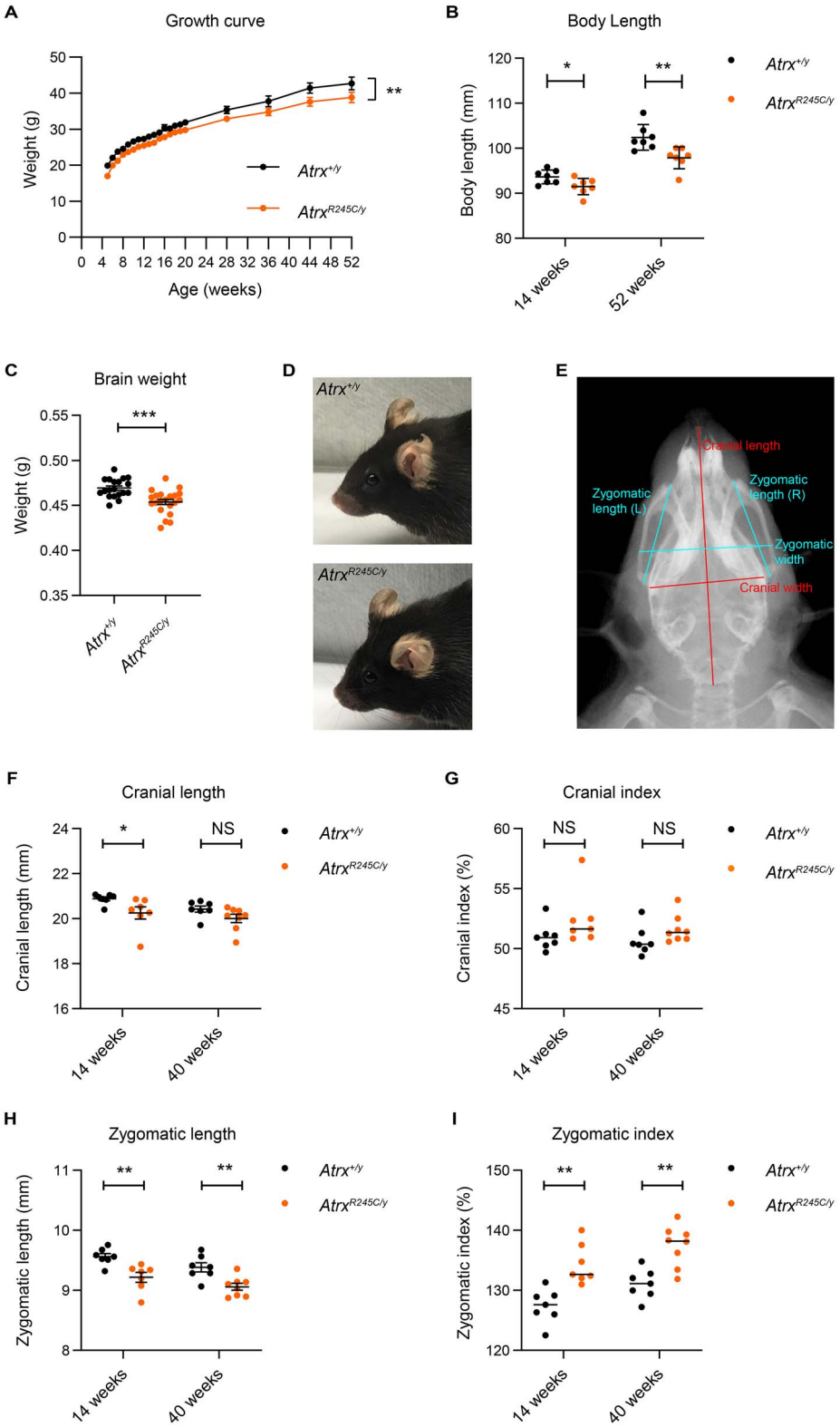

Figure 3. *Atrx*$^{R245C/y}$ mice have reduced body weight and craniofacial defects. (**A**) Growth curve showing body weight from 5 to 52 weeks of age (WT $n = 13$; R245C $n = 13$). Graph shows mean ± S.E.M. and genotypes were compared using repeated measures ANOVA: $^{**}P = 0.002$. (**B**) Body length (nose to base of tail) measured from X-ray analysis (WT $n = 7$; R245C $n = 7$). Genotypes were compared using *t*-tests: 14 weeks $^{*}P = 0.03$; 52 weeks $^{**}P = 0.007$. (**C**) Brain weight at 9 weeks (WT $n = 19$; R245C $n = 21$). Genotypes were compared using a *t*-test: $^{***}P = 0.0002$. (**D**) Representative photographs of the shortened snout phenotype observed in ~60% of *Atrx*$^{R245C/y}$ mice (lower), compared with WT controls (upper). (**E**) Example ventral X-ray of a WT mouse showing how cranial length, cranial width, zygomatic length (mean of left and right) and zygomatic width were measured. Cranial index [also known as cephalic index] (%) = cranial width/cranial length × 100 and zygomatic index (%) = zygomatic width/zygomatic length × 100. (**F–I**) X-ray analysis quantifying cranial length (F), cranial index (G), zygomatic length (H) and zygomatic index (I) at 14 weeks (WT $n = 7$; R245C $n = 7$) and 40 weeks (WT $n = 7$; R245C $n = 8$). Graphs of cranial length and zygomatic length show mean ± S.E.M. and genotypes were compared using *t*-tests: cranial length at 14 weeks $^{*}P = 0.47$; at 40 weeks $P = 0.099$; zygomatic length at 14 weeks $^{**}P = 0.004$; at 40 weeks $^{**}P = 0.004$. Graphs of cranial index and zygomatic index show median. Cranial index: genotypes were compared using a KS test at 14 weeks $P = 0.21$; and a *t*-test at 40 weeks $P = 0.14$. Zygomatic index: genotypes were compared using *t*-tests: at 14 weeks $^{**}P = 0.001$; at 40 weeks $^{**}P = 0.001$.

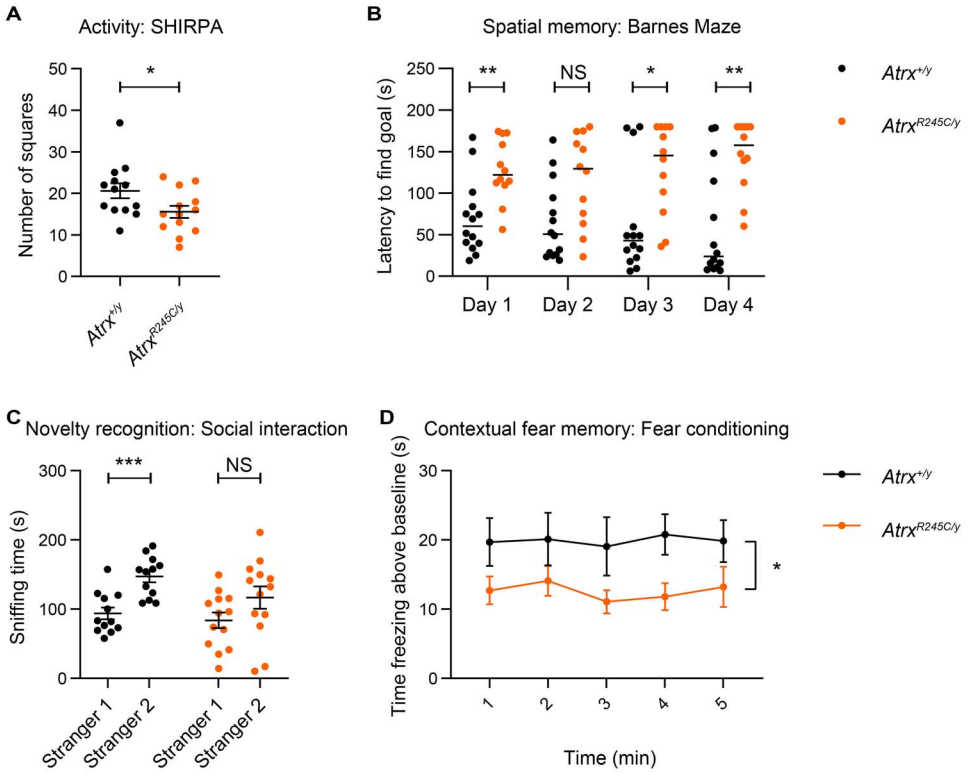

Figure 4. *Atrx*$^{R245C/y}$ mice have neurological defects. (**A**) Spontaneous activity assessed by number of squares entered in 30 s at 9 weeks of age (WT $n = 13$; R245C $n = 13$). Graph shows mean ± S.E.M. and genotypes were compared using a *t*-test: $^{*}P = 0.04$. (**B**) Mean latency to find the escape hole in the Barnes maze test in four trials was calculated for each of the 4 days of the experiment at 12 weeks (WT $n = 14$; R245C $n = 12$). Graphs show median and genotypes were compared using KS tests: day 1 $^{**}P = 0.004$, day 2 $P > 0.05$, day 3 $^{*}P = 0.014$, day 4 $^{**}P = 0.0096$. (**C**) Time spent sniffing a cylinder container a familiar (Stranger 1) or novel (Stranger 2) mouse in the three-chamber social interaction test at 10 weeks (WT $n = 12$; R245C $n = 13$). Graph shows mean ± S.E.M. and Stranger 1 versus 2 sniffing times were compared using paired *t*-tests: WT $^{***}P = 0.0004$, R245C $P > 0.05$. Genotypes were compared using two-way ANOVA: $P = 0.09$. (**D**) Contextual fear conditioning analysis at 13 weeks (WT $n = 14$; R245C $n = 13$). Time spent freezing (minus baseline determined before shock) when returned to the same contextual environment 24 h after receiving a foot shock. Graph shows mean ± S.E.M. and genotypes were compared using repeated measures ANOVA: $^{*}P = 0.025$.

escape hole with increasing ease, but mutants displayed impaired performance, which was significantly different from controls on three out of four days (Fig. 4B). Social Interaction was assessed in the three chamber test, where wild-type controls displayed a significant preference for the novel stranger mouse, but this was lost in the mutants (Fig. 4C). Given the results from the Barnes Maze and Social Interaction test, we asked whether defects in spatial memory and novelty preference affect the performance of *Atrx*$^{R245C/y}$ mice in the Y-maze. However, over the 8-min duration of this test, we saw no difference in Alternation index between genotypes (Supplementary Material, Fig. S4F). Lastly, in the Fear Conditioning paradigm, *Atrx*$^{R245C/y}$ mice showed impaired contextual but unaltered cued fear memory (Fig. 4D; Supplementary Material, Fig. S4G). We repeated some of these tests in late adult mice (around 1 year of age) and found a slight increase in hypoactivity (Supplementary Material, Fig. S5A and B) but no late-onset memory defects (Supplementary Material, Fig. S5C–F). Overall, our findings that *Atrx*$^{R245C/y}$ mice display neurological phenotypes that do not worsen with age are consistent with the classification of ATR-X syndrome as a developmental rather than degenerative condition.

Cerebellar volume is reduced in *Atrx*$^{R245C/y}$ mice

Perinatal lethality in mice lacking ATRX in the forebrain is associated with apoptotic cell death, resulting in reduced brain size, reduced cortical density and the replacement of the dentate gyrus of the hippocampus with a small mass of disorganized cells (8,26,30). In contrast, brains of the *Atrx*$^{R245C/y}$ mice show comparable morphology to controls at birth (Fig. 5A), and staining of cortical layer markers demonstrates that cellular differentiation in the cortex is unaffected and cell numbers are equivalent (Fig. 5B–D). These findings are consistent with normal head circumference at birth in ATR-X syndrome patients (27).

We therefore focused on the early adult timepoint, when *Atrx*$^{R245C/y}$ mice displayed neurological phenotypes (Fig. 4). MRI analysis revealed a slight downward trend in total brain volume at 9 weeks (Fig. 6A; −1.2% change, $P = 0.14$). Notably, this difference was not as robust as the decrease in the brain weight, measured at the same age in a separate cohort (Fig. 3C; −3.3% change, $^{***}P = 0.0002$). Reduced cortical thickness was not a contributing factor to microcephaly in adult mice, as this was only decreased in the ventral orbital cortex and was slightly, but significantly, increased in 8 out of the 38 cortical regions analysed (Supplementary Material, Fig. S6A). Published MRI analysis of patients' brains found a variety of grey and white matter abnormalities, most frequently non-specific brain atrophy (31). This was thought to be a result of reduced neuronal or glial production in the postnatal period rather than due to degeneration, though it has been reported to be progressive in two cases (31,32). Although affected brain regions vary among patients, there are several reports of partial or complete agenesis of the corpus callosum (27,31,33). To determine whether any regions are disproportionately smaller in the mutant mice, we performed comparative volumetric analysis on 183 brain

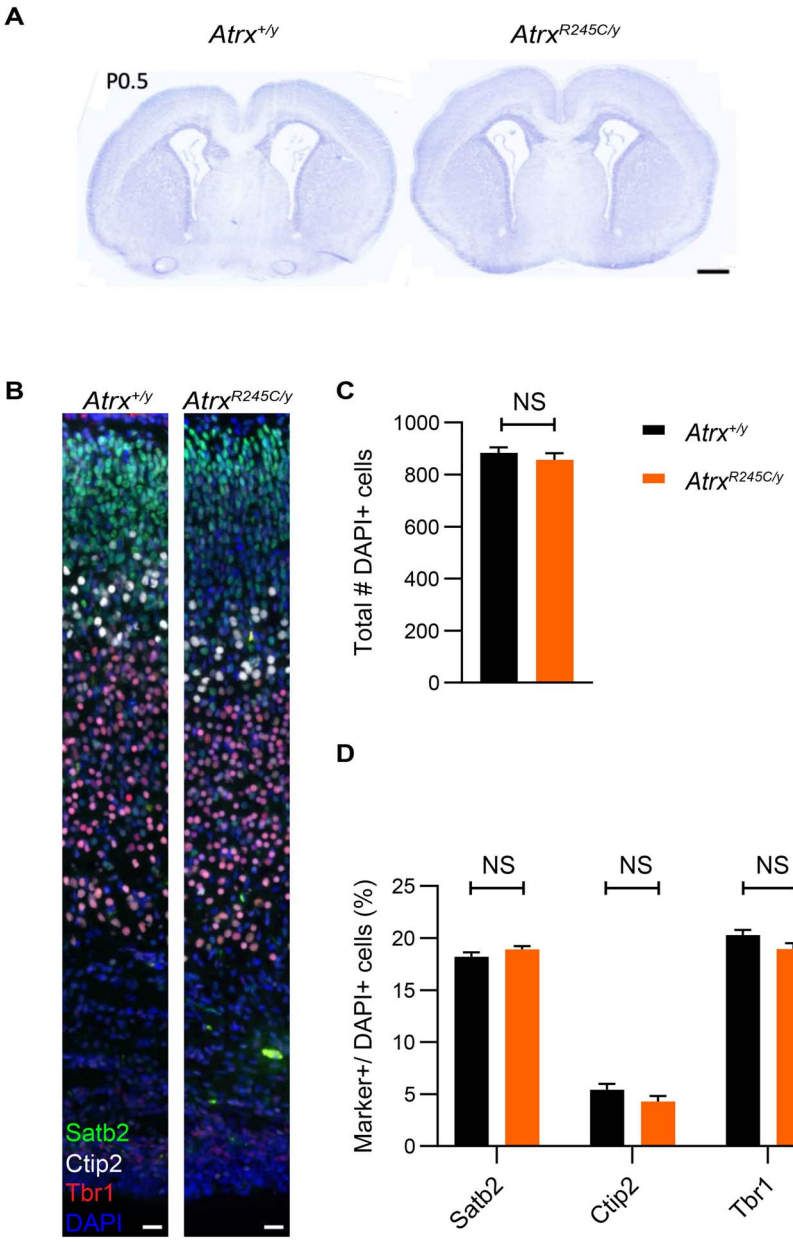

Figure 5. Embryonic cortical development is unaffected in *Atrx*$^{R245C/y}$ mice. (**A**) Representative images of a Nissl-stained coronal section (Bregma 0.62) from *Atrx*$^{+/y}$ and *Atrx*$^{R245C/y}$ mice at P0.5. Scale bar: 500 μm. (**B**) Representative images of P0.5 brain sections (Bregma −0.9 to −1.0) stained for cortical layer markers Tbr1 (red, layer VI), Ctip2 (white, layer V) and Satb2 (green, layers II–V). Nuclei are counterstained with DAPI (blue). Scale bar: 20 μm; $n = 4$. (**C**) Total number of DAPI-positive cells in the cortex ($n = 6$ biological replicates per genotype). (**D**) Quantification of layer marker + cells within the neocortex ($n = 6$ biological replicates per genotype). Graphs show mean ± S.E.M. and genotypes were compared using *t*-tests: all NS $P > 0.05$.

subregions. Using a significance threshold of $q < 0.1$ (after correction for multiple comparisons by the false discovery rate), 26 regions were smaller and four regions were larger in mutants than in wild-type littermate controls (Fig. 6B and C), consistent with a reduced brain size. This analysis did not detect a significant decrease in corpus callosum volume (Fig. 6C; Supplementary Material, Fig. S6B). However, quantification of corpus callosum thickness in rostral, medial and caudal histological sections revealed that it was significantly thinner in mutant mice in rostral (−12.3% change, $^{*}P = 0.02$) and medial (−28.0% change, $^{**}P = 0.002$) regions (Fig. 6D; Supplementary Material, Fig. S6C). Intriguingly, the MRI data revealed volumetric differences in regions of the cerebellum (Fig. 6B). Total cerebellar volume was significantly decreased (−6.0% change, $^{****}P < 0.0001$; Fig. 6D) and 17/39 regions in the cerebellum were significantly smaller (Fig. 6E; Supplementary Material, Fig. S6D and E). We therefore asked whether the reduced cerebellar volume was due to reduced cell number. Given that the cerebellum undergoes a period of rapid expansion in early postnatal development (34), it could be particularly susceptible to increased replicative stress in the mutants. From the analysis of cerebellar size using immunofluorescence staining, we observed a slight but not significant decrease in the area of cerebellar sections (Fig. 6G and H), reflecting the volumetric analysis. This was not accompanied by a significant decrease in the number of Purkinje (calbindin+) neurons (Fig. 6I), suggesting that a reduced cerebellar volume does not result from reduced proliferation or increased cell death.

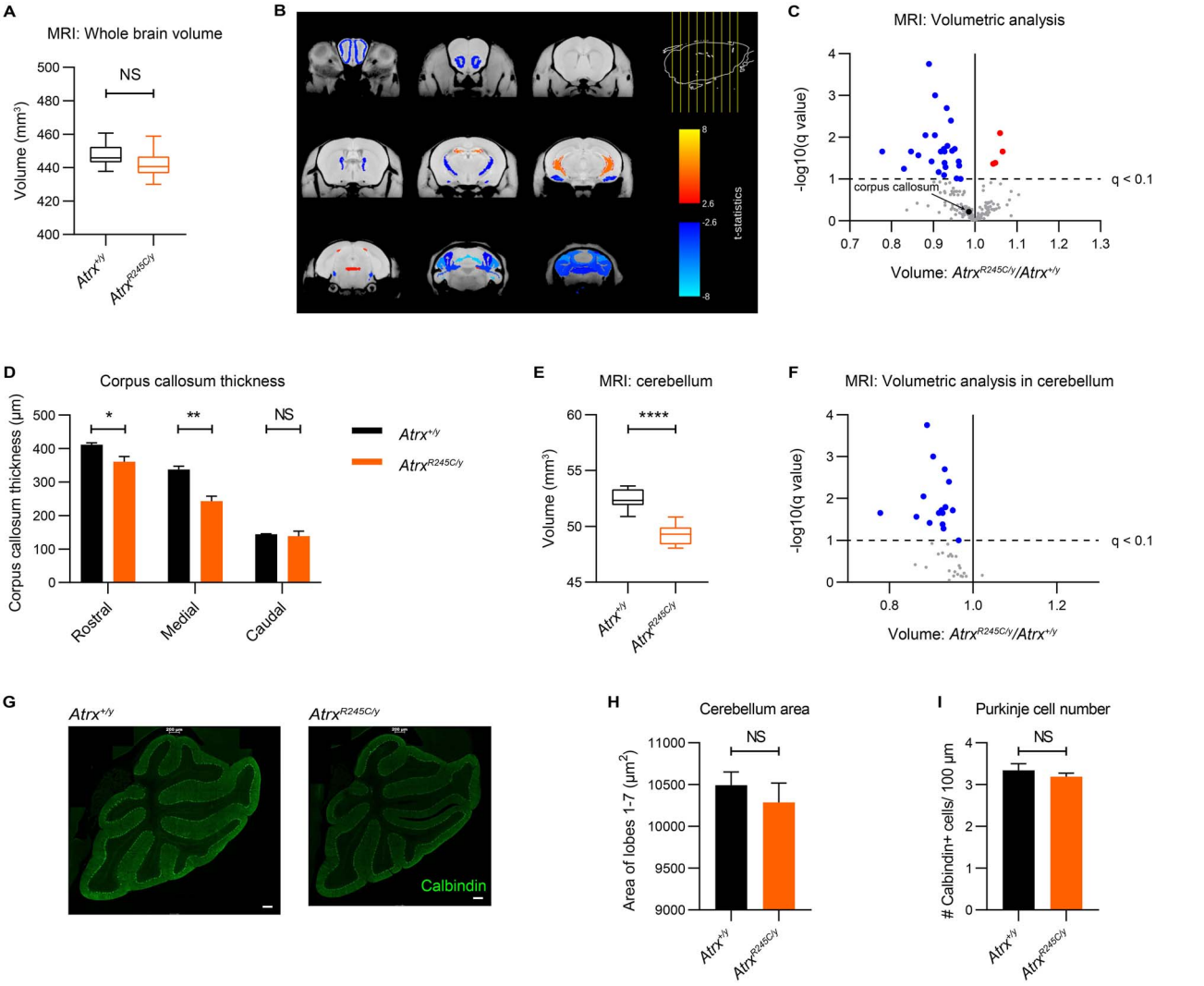

Figure 6. Cerebellar volume is reduced in *Atrx*$^{R245C/y}$ mice. (**A**) Whole brain volume analysed by MRI at 9 weeks (WT $n = 10$; R245C $n = 12$). Graph shows interquartile ranges and genotypes were compared using a *t*-test: $P > 0.05$. (**B**) Coronal sections showing significant changes in absolute volume in *Atrx*$^{R245C/y}$ mouse brains (coloured regions indicate significant changes at $q < 0.1$). (**C**) Volcano plot of all 183 brain regions. Significantly changed ($q < 0.1$) regions are highlighted in red (increased) and blue (decreased). The corpus callosum is highlighted in black. (**D**) Quantification of corpus callosum thickness measured from rostral, medial and caudal coronal brain sections stained with myelin-associated glycoprotein (MAG) at P40 (WT $n = 4$; R245C $n = 4$). The graph shows mean ± S.E.M. and genotypes were compared using *t*-tests: rostral $^{*}P = 0.023$; medial $^{**}P = 0.002$; caudal $P > 0.05$. (**E**) Total cerebellar volume analysed by MRI at 9 weeks (WT $n = 10$; R245C $n = 12$). Graph shows interquartile ranges and genotypes were compared using a *t*-test: $^{****}P < 0.0001$. (**F**) Volcano plot (as in Fig. 6C) showing volumetric analysis of the 39 cerebellar regions. (**G**) Representative images of cerebellar sections from WT and R245C mice at P40, stained with Calbindin, a marker of Purkinje neurons (green). Scale bar: 200 μm. (**H**, **I**) Quantification the total area of the cerebellar section (H) and the number of Calbindin+ cells per 100 μm across lobes I–VII (I) (WT $n = 3$; R245C $n = 3$). Graphs show mean ± S.E.M. and genotypes were compared using *t*-tests: both NS $P > 0.05$.

Mice lacking ATRX in postnatal forebrain excitatory neurons (via *CaMKII-Cre* mediated deletion) display similar neurobehavioural defects to those observed in *Atrx*$^{R245C/y}$ mice, including impaired spatial memory and contextual fear memory (10). *CaMKII-cKO* mice have reduced whole brain volume and differences in hippocampal neuroanatomy, consistent with the role of the hippocampus in memory and learning. MRI analysis showed that the total hippocampal volume is unaffected in *Atrx*$^{R245C/y}$ mice (Supplementary Material, Fig. S7A). We next compared our MRI volumetric analysis for hippocampal regions (*Atrx*$^{R245C/y}$ versus wild-type controls) with those reported for the *CaMKII-cKO* mice (versus wild-type controls). Of the seven regions affected in the *CaMKII-cKO* mice, three were also affected in the *Atrx*$^{R245C/y}$ mice, but in the opposite direction (Supplementary Material, Fig. S7B–D). We therefore found no correlation between the two models. We further analysed hippocampal structure by immunofluorescence staining and observed no differences in morphology (Supplementary Material, Fig. S7E). There were no differences in the proportion of total mature neurons (NeuN+) in the CA1, CA3 and dentate gyrus. Additionally, there were no differences in the total number of cells or the proportion of neuronal progenitor cells (doublecortin, DCX+) and interneurons (Calretinin+) in the dentate gyrus (Supplementary Material, Fig. S7F–H). In summary, changes in brain structure observed in *Atrx*$^{R245C/y}$ mice are distinct from those previously reported in *Foxg1*- and *CaMKII-cKO* models. Our brain morphology observations show overlap with the postnatal microcephaly and corpus callosum hypoplasia described in patients. Interestingly, this is the first report of reduced cerebellar volume in *Atrx*-mutant mice.

Atrx$^{R245C/y}$ neurons have reduced dendritic branching

To further address the cause of reduced brain size, we performed Sholl analysis on cultured hippocampal neurons derived from *Atrx*$^{R245C/y}$ mice and wild-type controls (Fig. 7A and B). Axon length was unchanged between genotypes, but total dendritic length was decreased in the mutant cells (Fig. 7C and D). This is consistent with a decrease in dendritic branching (Fig. 7E). It is therefore possible that microcephaly in *Atrx*$^{R245C/y}$ mice and ATR-X syndrome patients in part results from smaller, less complex cells.

Discussion

We present a mouse mutant containing the first engineered patient mutation as a novel model of ATR-X syndrome, carrying the most frequently occurring pathogenic variant: R246C. These mice recapitulate several morphological and neurological aspects of the disorder, including reduced body size, reduced brain weight, craniofacial defects and impaired brain function. These are reminiscent of the short stature, microcephaly, facial dysmorphism and intellectual disability described in patients (5,6). Overall, we found strong phenotypic overlap between the *Atrx*$^{R245C/y}$ mice and the "early truncating" model lacking exon 2, which were also characterized on C57BL/6J (24,25). Specifically, both models have reduced body weight, brain weight, impaired spatial memory in the Barnes Maze, impaired novelty preference (analysed using the Social Interaction test for *Atrx*$^{R245C/y}$ and the Novel Object Recognition test for *Atrx*$^{\Delta ex2/y}$) and impaired contextual fear memory. Although defects in spatial memory and/or novelty preference displayed by the *Atrx*$^{\Delta ex2/y}$ mice were also evident as decreased Alternation index in the Y-maze, this result wasn't reproduced in the *Atrx*$^{R245C/y}$ mice. Historically, patients with different mutations in the same gene have often been categorized as having distinct conditions, sometimes with unique names. This has been the case for ATR-X syndrome: for example, some patients with the "early-truncating" mutation R37X were reported to have Chudley-Lowry syndrome (35). The presence of a phenotypic signature shared by both mouse models carrying hypomorphic alleles of *Atrx* supports the move in the rare disease field towards categorizing genetic diseases by the affected gene.

This is the first report of a craniofacial phenotype (shortened snout) in a mouse model with reduced ATRX function. Intriguingly, transgenic mice overexpressing ATRX have a similar phenotype (36). Further work is needed to determine the mechanism by which ATRX dosage affects skull morphology and whether the penetrance of the shortened skull phenotype could be modified by backcrossing to other strains.

We found that the *Atrx*$^{R245C/y}$ mice did not recapitulate the alpha-thalassemia, genital abnormalities or muscle hypotonia described in patients. The absence of the first two features can be explained by the lack of the G-rich Ψζ VNTR repeat, previously linked to ATRX-mediated alpha-globin gene regulation, at the mouse locus (29) and the connection between genital abnormalities and C-terminal mutations (5,19). The absence of muscle defects in *Atrx*$^{R245C/y}$ mice was surprising, as deletion of *Atrx* in skeletal muscle (via *Myf5-Cre* mediated excision) resulted in neonatal hypotonia and impaired recovery after chronic exercise-induced damage (14,15). It is possible that the hypomorphic allele (R245C) retains enough functionality to rescue these phenotypes on C57BL/6J, but they could be detectable on another background strain. In support of this, the commonly used model of Duchenne Muscular Dystrophy (DMD), *Dmd*^{mdx}, which carries a truncated *DMD* allele, is minimally affected on several background strains including C57BL/10 but displays severe muscular dystrophy on DBA/2J (37). The ameliorating effect of the background was overcome by removing residual DMD activity, as demonstrated in a recently published *DMD* knockout model, *Dmd*^{em1Rcn} on C57BL/6J (38). This could also explain why the muscle phenotypes displayed by the *Atrx Myf5-cKO* mice were not detected in *Atrx*$^{R245C/y}$ mutants.

Atrx$^{R245C/y}$ mice can now be adopted by the field to further our understanding of the molecular mechanisms underlying ATR-X syndrome and to test potential therapeutic avenues. ATRX is believed to be a pleiotropic protein, due to its proposed roles in multiple molecular processes. Notably, these studies have been restricted to accessible patient cells (erythroblasts and lymphoblastoid cells), knock-out cell lines and tissues derived from conditional knock-out mice (7,8,29,39). Our mice carry a constitutive hypomorphic mutation, representing the genetic status of all ATR-X patients. We have shown here that this model better represents patient disease pathology than *Atrx* conditional knock outs: *Atrx*$^{R245C/y}$ mice survive to adulthood, do not exhibit extensive neuronal cell loss and display neurobehavioural phenotypes. The reduction in the dendritic length and branching suggests that acquired microcephaly in patients could be related to abnormal neuronal morphology. Interestingly, the reduced brain weight phenotype in *Atrx*$^{\Delta ex2/y}$ mice is accompanied by altered dendritic spine density (25). Further work is needed to determine whether these models share these cellular phenotypes.

We found that ATRX[R245C] mutant protein is sufficient to rescue the neuronal death phenotype present in mice lacking ATRX in the forebrain. This is supported by a recent study using CRISPR-edited mouse ESC-derived neural progenitor cells (NPCs) where a cell death phenotype was observed in cells lacking ATRX, but not in those expressing a stable ATRX mutant with two amino acid changes in the ADD domain that specifically abolish heterochromatin binding (40). This raises the question whether ATRX[R245C] can also rescue the replicative stress phenotype described in *Atrx-null* NPCs (41) and myoblasts (14). Having a well-characterized patient-relevant mouse model of ATR-X syndrome means that we can investigate the role of ATRX protein in replication and other molecular processes in the most relevant tissues and developmental time points. This will help us understand which aspects of ATRX protein function are "missing" to result in ATR-X syndrome; and how residual functionality of a hypomorphic mutant rescues the more severe *Atrx*-null phenotypes. We predict that such studies will uncover molecular phenotypes shared across ATR-X syndrome-causing mutants, and those specific to ATRX[R245C] or ADD mutants. Dissecting the functionality of the ADD domain in heterochromatin maintenance, gene regulation and DNA damage repair is of particular interest as 43% of patients have mutations that lie within it. ATRX has historically been regarded as a heterochromatin protein, recruited to pericentromeric foci via the affinity of the ADD domain for H3K9me3 (42). This recruitment is severely disrupted by the R245C mutation, but it is possible that ATRX[R245C] persists at a subset of heterochromatic loci due to recruitment via its interaction partners, such as HP1 and MeCP2. Furthermore, a recent study demonstrated that ATRX is also found at active chromatin sites, such as promoters and enhancers (39), where the recruitment mechanism is yet to be determined. ATRX[R245C] retains both the ATPase and DAXX interaction domains, suggesting that if it were able to be recruited to genomic sites, it could remodel chromatin and incorporate histone H3.3.

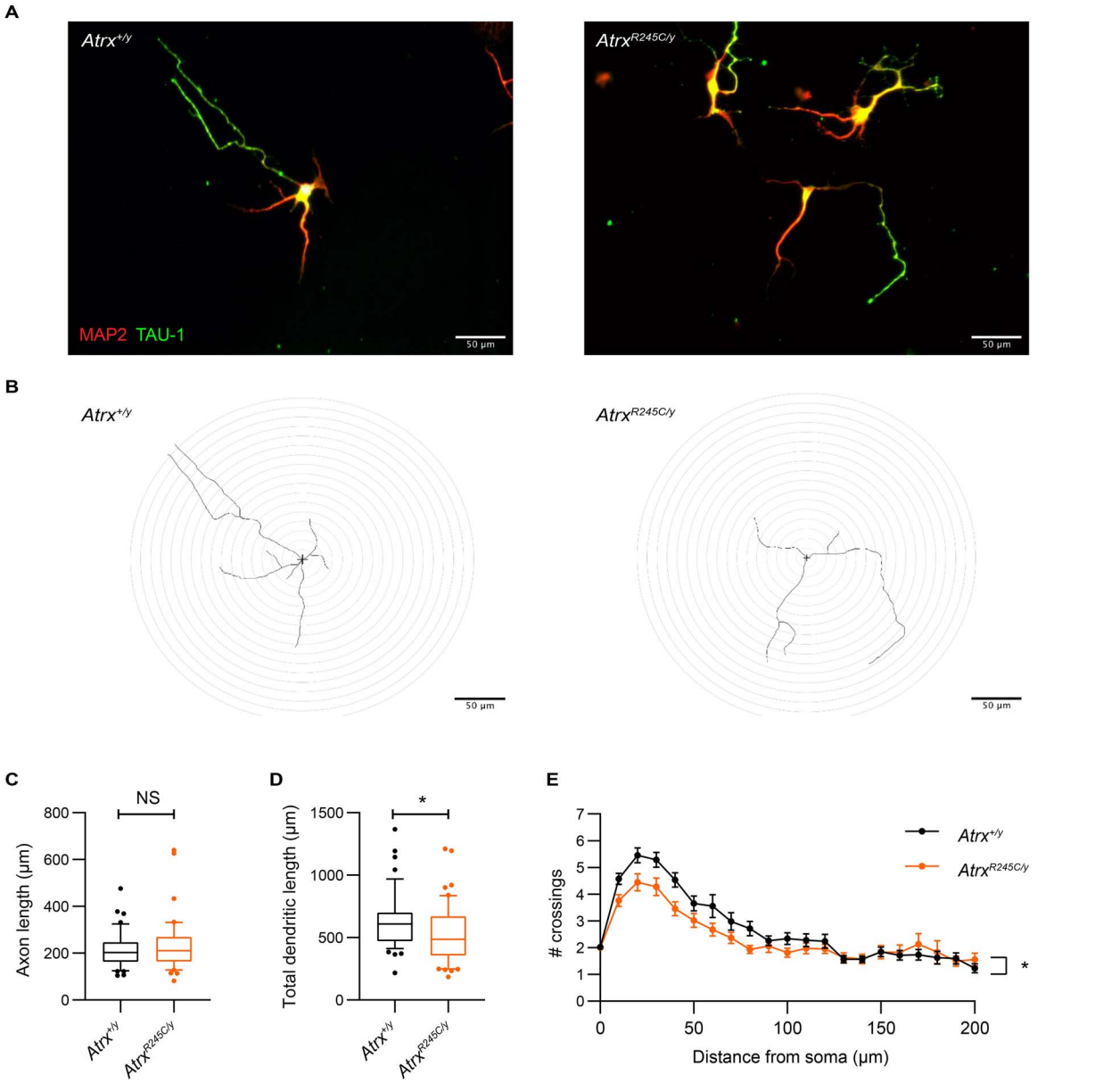

Figure 7. *Atrx*$^{R245C/y}$ neurons have reduced dendritic length and branching. (**A**) Hippocampal neurons derived from *Atrx*$^{+/y}$ and *Atrx*$^{R245C/y}$ mice at E17.5 (DIV5) stained with MAP2 (red) and TAU-1 (green). (**B**) Representative tracings of the neurons shown in (A), used for Sholl analysis. (**C**, **D**) Axon length (C) and total dendritic length (D) of the neurons (WT $n = 49$; R245C $n = 50$). Graphs show interquartile ranges (whiskers 10–90 percentile) and genotypes were compared using KS tests: axon length $P > 0.05$; total dendritic length $^*P = 0.043$. (**E**) Sholl analysis of dendritic branching in the same cells. Graph shows mean ± S.E.M. for each distance, and genotypes were compared using Mixed-Effects analysis: $^*P = 0.015$.

A patient-relevant mouse model is crucial for therapeutic studies. Our extensive phenotypic characterization of this model has identified key behavioural paradigms to be used when assessing phenotypic rescue. The strong phenotypic overlap between the *Atrx*$^{R245C/y}$ and *Atrx*$^{\Delta ex2/y}$ models supports the relevance of these tests for treating patients carrying all types of ATRX mutations.

Materials and Methods

Experimental model and subject details

Mouse lines

Animal procedures were approved by the Animal Use Committees at the Canadian Council on Animal Care-accredited animal facilities, The Centre for Phenogenomics (TCP) and the University of Ottawa. All mice were housed in specific-pathogen-free facilities. They were maintained on a 12-h light/dark cycle and given ad libitum access to food and water. Mice were fed a standard diet (HarlanTeklad 2918), consisting of 18% protein, 6% fat and 44% carbohydrates. They were housed in individually ventilated cages (IVC) with wood chippings, tissue bedding and additional environmental enrichment in groups of up to five animals. Mutant mice were housed with their wild-type littermates. *Atrx*^{em1Tcp} (*referred to as* *Atrx*^{R245C}) mice were generated in this study by the TCP Model Production Core via CRISPR/Cas9-meditated editing in C57BL/6J zygotes (detailed method described below). The *Atrx*^{em1TCP} mouse line will be available from the Canadian Mutant Mouse Repository (CMMR). Heterozygous *Atrx*$^{R245C/+}$ females were crossed with wild-type C57BL/6J males to produce hemizygous *Atrx*$^{R245C/y}$ males and *Atrx*$^{+/y}$ littermate controls for all experiments.

Cohort 1 ($Atrx^{+/y}$ $n=13$; $Atrx^{R245C/y}$ $n=13$) underwent body weight measurements (5–52 weeks), SHIRPA (9 weeks), Social Interaction (10 weeks), Y-maze (11 weeks), Accelerating Rotarod (13 weeks), SHIRPA (55 weeks), gait analysis (55 weeks), grip strength measurement (55 weeks) and Fear Conditioning (56 weeks). Cohort 2 ($Atrx^{+/y}$ $n=14$; $Atrx^{R245C/y}$ $n=13$) underwent Open Field (9 weeks), Light/Dark box (10 weeks), gait analysis (10 weeks), Barnes Maze (12 weeks), Fear Conditioning (13 weeks) and complete blood counts (14 weeks). Cohort 3 ($Atrx^{+/y}$ $n=11$; $Atrx^{R245C/y}$ $n=9$) underwent grip strength measurement (3 weeks) and chronic exercise (13 weeks). Cohort 4 ($Atrx^{+/y}$ $n=13$; $Atrx^{R245C/y}$ $n=12$) underwent Elevated Zero Maze (9 weeks), grip strength measurement (9 weeks) and MRI (9 weeks). Cohort 5 ($Atrx^{+/y}$ $n=9$; $Atrx^{R245C/y}$ $n=9$) underwent Open Field (55 weeks), Y-maze (55 weeks) and Accelerating Rotarod (55 weeks). Cohort 6 ($Atrx^{+/y}$ $n=5$; $Atrx^{R245C/y}$ $n=5$) underwent DEXA (3 weeks). Cohort 7 ($Atrx^{+/y}$ $n=3$; $Atrx^{R245C/y}$ $n=11$) underwent grip strength measurement (3 weeks) and X-ray analysis (3 weeks; $Atrx^{+/y}$ $n=3$; $Atrx^{R245C/y}$ $n=5$). Cohort 8 ($Atrx^{+/y}$ $n=7$; $Atrx^{R245C/y}$ $n=7$) underwent X-ray analysis (14 and 52 weeks). Cohort 9 ($Atrx^{+/y}$ $n=7$; $Atrx^{R245C/y}$ $n=8$) underwent X-ray analysis (40 weeks).

Method details

Generation of $Atrx^{em1Tcp}$ (referred to as $Atrx^{R245C}$) knock-in mice

$Atrx^{em1Tcp}$ mice were generated by the Model Production Core at TCP by Cas9 endonuclease and a guide RNA with the spacer sequence CCTTTCGACCAAGGTTGCGC and a single-strand oligonucleotide encoding the changes c.733C>T, p.R245C and c.729C>T, p.I243I to introduce the patient mutation and inactivate the PAM sequence in ENSMUST00000113573 (NM_009530), encoding NP_033556. These reagents were introduced into C57BL/6J zygotes via electroporation (43) and maintained on this background by crossing heterozygous $Atrx^{R245C/+}$ females with wild-type C57BL/6J males.

Introduction of the desired mutations was assessed in founders and all N1 heterozygous $Atrx^{R245C/+}$ females by Sanger sequencing after PCR amplification. Copy number was analysed in all N1 heterozygous $Atrx^{R245C/+}$ females by qPCR amplification of PCI-purified genomic DNA (diluted to 2.5 ng/μl) to verify that no additional copies of the donor oligonucleotide had integrated. The ATRX locus was detected with qATRX F and qATRX R primers (which lie within the donor oligonucleotide). Values were normalized to the TFRC locus, amplified with qTFRC F and qTFRC R primers. qPCR was performed on a Viia7 instrument (ABI) instrument using SYBR Green PCR Master Mix (Invitrogen). PCR amplification conditions: annealing temperature 58°C, 40 cycles. Relative abundance $= E^{TFRC\wedge CT^{TFRC}}/E^{ATRX\wedge CT^{ATRX}}$. Abundance was normalized to the mean of three wild-type females. See Supplementary Material, Table S1 for primer sequences. Genotype ratios of N2 and N3 pups were analysed using Fisher's exact tests.

Genotyping

Tail tip genomic DNA was PCR amplified with ATRX_RC gen F and ATRX_RC gen R primers and digested with FspI (NEB R0135S). FspI cuts the wild-type allele (product sizes: 245 + 120 bp), but the restriction site is lost in the R245C allele (product size: 365 bp). See Supplementary Material, Table S1 for primer sequences.

Neuronal cell cultures

Cortical and hippocampal neuron cultures were prepared from E17.5 mouse embryos (44). Briefly, embryos were individually decapitated and cortex or hippocampi were dissected and collected in cold Hank's balanced salt solution (HBSS: NaHCO3 4.2 mM, Hank's salt powder 0.952%, HEPES 12 mM, 4-(2-hydroxyethyl)-1-piperazineethane-sulphonic acid, Sigma), then digested with 0.25% Trypsin at 37°C for 8 min. Enzymatic digestion was blocked with Dulbecco's Modified Eagle Medium high glucose (DMEM), supplemented with 10% Fetal Bovine Serum (FBS) and penicillin-streptomycin. The tissue was centrifuged at 800 rpm for 5 min at room temperature. The tissue was resuspended with DMEM + 10% FBS and mechanically triturated. Hippocampal neurons were plated on 12 mm cover glasses and cortical neurons directly on polystyrene multiwell plates, coated with 1 mg/ml poly-L-lysine (Sigma). Cultures were grown at 37°C and 5% CO_2 in Neurobasal Medium (Invitrogen) supplemented with 2% B-27 (Invitrogen), 1 mM L-glutamine and 1% penicillin-streptomycin. Genotype and sex were later confirmed by PCR.

RNA purification and qPCR

Cortices were dissected from $Atrx^{R245C/y}$ mice and $Atrx^{+/y}$ littermate controls at P0.5 and P60. RNA was isolated using Trizol (Thermo Fisher Scientific #15596026) according to the manufacturer's instructions. 2 μg of total RNA was used for DNase treatment using DNA-free™ DNA Removal Kit (Fisher #AM1906) and then reverse-transcribed to cDNA using RevertAid Reverse Transcriptase (Fisher #EP0442) according to the manufacturer's instructions. Synthesized cDNA was further diluted 1:10 for qPCR. RT-qPCR analysis was carried out using the Lo-Rox SYBR 2× mix (FroggaBio Inc #CSA-01195) under the following conditions: one cycle at 95°C for 1 min, and then 40 consecutive cycles at 95°C for 10 s, 60°C for 10 s and 72°C for 20 s using AriaMx Real-Time PCR System (Agilent). All primers (Supplementary Material, Table S1) were verified by melt curve analysis after qPCR amplification. The ΔΔCt method was used to compare fold-change. GAPDH was used for normalization. Triplicate or quadruplicate samples were performed per reaction and a minimum of 3 mice analyzed per genotype. Student's *t*-test was used for statistical significance.

Whole blood was collected from the saphenous vein in EDTA at 18 weeks ($Atrx^{+/y}$ $n=3$; $Atrx^{R245C/y}$ $n=6$). In sum, 100 μl whole blood was homogenized in 1 ml QIAzol (Qiagen) using a TissueLyser II (Qiagen) at 20 Hz for 3 min. Samples were incubated at room temperature for 5 min before 200 μl chloroform was added. Samples were centrifuged at 12 000*g* for 15 min at 4°C and the upper phase was transferred to a new tube. RNA was precipitated with 600 μl 70% ethanol and isolated in a RNeasy Mini Spin Column. RNA was purified using the RNeasy kit (Qiagen 74106) according to manufacturer's instructions. In short, the RNA was washed with the 700 μl Buffer RW1, then 2× 500 μl Buffer RPE, and eluted in 50 μl RNAse-free water. gDNA removal and cDNA synthesis was performed on 1.25 μg RNA using SuperScript™ IV VILO™ Master Mix with ezDNase™ Enzyme (Thermo Scientific 11766050) according to manufacturer's instructions. cDNA was diluted 1 in 1000 for the analysis of α-globin expression by qPCR amplified with qHba-a1/2 F and qHba-a1/2 R, normalized to β-globin expression amplified with qHbb F and qHbb R. See Supplementary Material, Table S1 for primer sequences. PCR amplification conditions: annealing temperature 60°C, 40 cycles. Relative abundance $= E^{Hbb\wedge CT^{Hbb}}/E^{Hba\wedge CT^{Hba}}$. Genotypes were compared using *t*-tests (unpaired, two-tailed).

Protein purification and western blotting

Cortices were quickly dissected, snap frozen in liquid nitrogen, and then homogenized in ice-cold RIPA buffer (10 mM Tris-Cl, pH8.0, 1 mM EDTA, 1% Triton X-100, 0.1% sodium deoxychlorate,

0.1% SDS, 140 mM NaCl and 1 mM PMSF) supplemented with protease inhibitor cocktail (Sigma-Aldrich). After 20 min incubation on ice, samples were centrifuged (17 000g for 20 min) and the protein supernatant quantified by Bradford assay. Protein samples were resolved on sodium dodecyl sulfate polyacrylamide gels under denaturing conditions and blotted onto PVDF membranes (Immobilon-P; Millipore, Burlington, MA, United States) by wet transfer for 1–2 h at 90 V. Membranes were blocked (45 min, room temperature) with 5% skim milk in TBST (Tris-buffered saline containing 0.05% Triton X-100), and incubated (4°C, overnight) with the following antibodies: mouse anti-ATRX 39F (1:1000), anti-NeuN (1:750; Millipore, #MAB377) dilution and mouse anti-Vinculin (1:10 000; Sigma-Aldrich #V9131). Membranes were incubated (1 h, room temperature) with HRP-conjugated goat anti-Rabbit IgG (Sigma #A4914), sheep anti-mouse (Sigma #A5906) or goat anti-rat (Sigma #AP136P) secondary antibodies (1:2000 to 1:30 000). Membranes were washed 5 × 5 min in TBST and signals were detected using the Clarity Western ECL Substrate (Biorad #1705060). At least two separate gels were immunoblotted with cortical extracts from independent litters and used for quantitation.

Cycloheximide assay

For the analysis of protein stability, cultures were treated with vehicle (DMSO) or 100 μM CHX (Sigma) for 0, 3 and 8 h. Cells were lysed in RIPA lysis buffer and protein was collected for western.

Nissl staining and immunofluorescence

Nissl staining was performed using cresyl violet standard staining procedures. In brief, 12 μm frozen coronal sections (0.62 mm from Bregma) were rehydrated in 95, 70 and 50% ETOH (ethanol) for 10, 1 and 1 min, respectively, and then incubated in ddH2O for 2 × 5 min. Rehydrated sections were then stained in 1% cresyl violet acetate staining solution (1% cresyl violet, 0.25% glacial acetic acid) for 4 min. After 5 min washing in ddH2O, the sections were dehydrated in 50, 70, 95 and 100% ETOH for 2, 2, 2 and 5 min, respectively. Sections were then cleared by incubation in xylene for 3 × 5 min, mounted with Permount and visualized under Axio Scan. Z1 (Zeiss) scanning microscope.

Postnatal day 0.5 (P0.5) brain sections (12 μm at −0.9 to −1.0 from Bregma) were washed 3 × 5 min in PBST (PBS with 0.1% Triton X-100) prior to blocking or antigen retrieval. For antigen retrieval, slides were submerged in citrate buffer (10 mM citrate, 0.05% Tween-20, pH 6.0) and heated in a microwave (power level 2) for 10 min. Slides were blocked for 1 h at room temperature in 10% horse serum/PBST, and then incubated (overnight, 4°C) with primary antibodies. The following primary antibodies were used at 1:200, unless indicated: rabbit anti-Tbr2 (Abcam #37003); rabbit anti-Pax6 (1:100; Abcam #195045); mouse anti-SATB2 (1:50; Abcam #51502); rat anti-Ctip2 (Abcam #18465); rabbit anti-Tbr1 (Abcam #31940); mouse anti-ATRX (39F; (45)). The following day, sections were washed 4 × 5 min in PBST and then incubated with DyLight488, DyLight594, or DyLight649-conjugated secondary antibodies (1:500; Jackson ImmunoResearch, PA). All sections were counterstained with Hoescht 33342 dye (Thermo Fisher Scientific) and coverslips were mounted with Dako Fluorescence Mounting Medium (Dako Canada, ON).

Morphological and muscle function analysis

Dual-energy X-ray absorptiometry (DEXA) was performed on anaesthetized mice by the TCP Clinical Phenotyping Core at 21 days of age ($Atrx^{+/y}$ $n = 5$; $Atrx^{R245C/y}$ $n = 5$). X-rays were performed on anaesthetized mice (Faxitron MX-20) by the TCP Clinical Phenotyping Core at 3 weeks ($Atrx^{+/y}$ $n = 3$; $Atrx^{R245C/y}$ $n = 5$); 14 and 52 weeks ($Atrx^{+/y}$ $n = 7$; $Atrx^{R245C/y}$ $n = 7$) and 40 weeks ($Atrx^{+/y}$ $n = 7$; $Atrx^{R245C/y}$ $n = 8$).

Grip strength was measured on a Grip Strength Meter (Bioseb) using three separate cohorts aged 3 weeks ($Atrx^{+/y}$ $n = 14$; $Atrx^{R245C/y}$ $n = 20$), 9 weeks ($Atrx^{+/y}$ $n = 13$; $Atrx^{R245C/y}$ $n = 12$) and 52 weeks ($Atrx^{+/y}$ $n = 13$; $Atrx^{R245C/y}$ $n = 13$). Settings: GF (gram-force); mode = T-PK. Animals were placed with their torso parallel to the grid (no mesh on grid) and allowed to attach before pulling backwards over the grid by its tail. The mean of three measurements for fore + hindlimbs was calculated and normalized by body weight. Gait was analysed on a DigiGait treadmill (Mouse Specifics, Inc.) using two separate cohorts aged 10 ($Atrx^{+/y}$ $n = 13$; $Atrx^{R245C/y}$ $n = 13$) and 55 weeks ($Atrx^{+/y}$ $n = 13$; $Atrx^{R245C/y}$ $n = 10$, as 3/13 $Atrx^{R245C/y}$ animals failed to walk on the treadmill). 5–8 s of continuous movement were recorded at 19 cm/s (no slope). Videos were analysed using DigiGait Analysis 15 software. A cohort of mice underwent chronic exercise on a treadmill (Columbus Instruments 1055SRM Exer-3/6 Open Treadmill) at 13 weeks ($Atrx^{+/y}$ $n = 11$; $Atrx^{R245C/y}$ $n = 9$). Mice were acclimatized to the treadmill over four training days: day 1 = 3 m/min for 1 min, no slope; day 2 = 3 m/min for 1 min then 4 m/min for 1 min, 5° decline; day 3 = 3 m/min for 1 min, 4 m/min for 1 min then 5 m/min for 1 min, 10° decline; and day 4 = 3 m/min for 1 min, 4 m/min for 1 min, 5 m/min for 1 min, then 6 m/min for 3 min, 15° decline; before undergoing trials for 3 days (days 5–7): each 3 m/min for 1 min, 4 m/min for 1 min, 5 m/min for 1 min, 6 m/min for 3 min, 8 m/min for 0.5 min, 10 m/min for 0.5 min then 12 m/min for 10 min, 15° decline. Animals were manually kept on the treadmill by the experimenter (shock grids were not used) and monitored for signs of exhaustion, at which point they were returned to their home cage to recover. Mice were injected with Evans Blue Dye (1% w/v in PBS) via IP (10 μl/g body weight) after the second trial day to visualize muscle damage. TA muscle was harvested, coated in OCT and snap-frozen in isopentane chilled in liquid nitrogen. Muscle tissue from the worst three performing animals per genotype (to maximize the chance of identifying damage) was sectioned at 8 μm on a Cryostat for analysis. Infiltration of Evans Blue Dye was analysed by fluorescence microscopy (not detected). Muscle sections were stained with hematoxylin and eosin (H&E) and slides were then scanned using the 3DHPannoramic Slide Scanner by the Imaging Facility at the Hospital for Sick Children. SlideViewer (3DHISTECH) was used for image acquisition. Feret's diameter was analysed using Image J to quantify MinFeret ($n = 300$ myofibres per animal).

Magnetic resonance imaging (MRI)

MRI for assessment of brain morphology was performed *in vivo* at the Mouse Imaging Centre using multiple-mouse MRI, imaging up to four mice simultaneously (46,47). Twenty-four hours prior to scanning, mice received an intraperitoneal injection of 30 mM $MnCl_2$ (0.4 mmol per kg; M8054, Sigma-Aldrich). During the MRI scan, mice were anesthetized with isoflurane (1–1.5%) and monitored based on their respiratory signal (48). Gradient-echo images were acquired with the following parameters: TR = 26 ms; TE = 8.25 ms; two averages; 334 × 294 × 294 matrix size; 25 × 22 × 22 mm^3 field of view; 75 μm isotropic voxel size; and a total acquisition time of 1 h using a "cylindrical" masking of k-space (49).

Haematology

Complete blood counts were performed by the TCP Clinical Phenotyping Core. Genotypes were compared using *t*-tests (unpaired, two-tailed).

Behavioural analysis

Modified SHIRPA (SmithKline Beecham, Harwell, Imperial College, Royal London Hospital, phenotype assessment) screening was performed on the same cohort at 9 and 55 weeks of age ($Atrx^{+/y}$ $n = 13$; $Atrx^{R245C/y}$ $n = 13$). Animals were assessed for appearance, spontaneous locomotor activity (number of squares entered with all four paws in a 51 cm × 37 cm arena marked with 15 equal squares over 30 s), gait, reflexes (startle response, touch escape, righting reflex, contact righting reflex in plastic tube, visual placing, pinnal reflex, corneal reflex, response to tail pinch and pupillary light reflex), and behaviour during screen and when handled (passivity, trunk curl, limb grasping, biting and vocalization). Open Field was performed on two independent cohorts at 9 weeks ($Atrx^{+/y}$ $n = 12$; $Atrx^{R245C/y}$ $n = 13$) and 55 weeks ($Atrx^{+/y}$ $n = 9$; $Atrx^{R245C/y}$ $n = 9$). Animals explored an evenly lit (200 lux) 43.5 cm × 43.5 cm arena for 20 min and their movement was detected using 16 beam IR arrays (X and Y axes). Data were processed using Activity Monitor software. The centre of the area was defined as the central 40% of the total area. The Light/Dark test was performed at 9 weeks ($Atrx^{+/y}$ $n = 13$; $Atrx^{R245C/y}$ $n = 13$). Lidded dark box inserts were added to the Open Field arena (50% of arena area). Animals were placed in the dark half and allowed to explore for 15 min and their movement was detected using 16 beam IR arrays (x and y axes). Data were processed using Activity Monitor software. The Elevated Zero Maze was performed at 9 weeks ($Atrx^{+/y}$ $n = 12$; $Atrx^{R245C/y}$ $n = 12$). Animals explored a "O" shaped maze with diameter 60 cm and path width 7 cm, divided into four equal quadrants: two open quadrants and two walled quadrants, elevated 70 cm off the floor for 5 min. Behaviour was monitored and analysed using Ethovision XT 13 software (Noldus). The 3-day accelerating rotarod test was performed on two independent cohorts at 13 weeks ($Atrx^{+/y}$ $n = 13$; $Atrx^{R245C/y}$ $n = 13$) and 55 weeks ($Atrx^{+/y}$ $n = 8$; $Atrx^{R245C/y}$ $n = 9$). Animals were placed onto a rod facing forwards on the apparatus (Accelerating RotaRod for 5 mice LE8200, Harvard Apparatus Canada). The motor was then started on acceleration mode from 4 to 40 rpm over 5 min. The latency to fall for each trial was recorded. Each day consisted of four trials, separated by an intertrial interval of 30–45 min. Baseline motor function was assessed on day 1 and motor learning ability was assessed over the total 3 days. Barnes maze analysis was performed at 12 weeks ($Atrx^{+/y}$ $n = 14$; $Atrx^{R245C/y}$ $n = 12$) over 5 consecutive days. The maze consisted of a circular white evenly lit (∼75 lux) platform (121 cm in diameter) elevated ∼1 m from the floor with 40 equally spaced holes around the periphery. A black escape box was placed under one hole and shallow black boxes were placed under the remaining holes. The maze was surrounded by four spatial clues to aid orientation. On day 1, mice were placed into a cylindrical holder in the centre of the maze and released after 10 s to explore and find the escape box for a maximum of 3 min. If the subject did not enter the escape box, it was gently guided by the experimenter. Mice were allowed to stay in the escape box for 10 s. On days 2–5, mice underwent four trials (with an intertrial interval of 2 h), where they were given a maximum of 3 min to enter the escape box. If the subject did not enter the escape box, it was gently guided by the experimenter. Mice were allowed to stay in the escape box for 10 s. For all trials, music was played from when the mouse was released until it entered the escape box. Behaviour was monitored and analysed using Ethovision XT 14 software (Noldus) using three-point tracking. Social novelty was assessed at 10 weeks ($Atrx^{+/y}$ $n = 12$; $Atrx^{R245C/y}$ $n = 13$) in an arena comprising three equal chambers. Animals were first acclimatized to the empty arena for 5 min. In Session I, two cups were added in opposite corners one of which contained "stranger 1" and animals were released from the central chamber and allowed to explore for 10 min. In Session II, "stranger 1" remained in place and "stranger 2" was added to the second cup and animals were released from the central chamber and allowed to explore for 10 min. All strangers used were male C57BL/6J mice around 10 weeks of age. Behaviour was monitored and analysed using Ethovision XT 13 software (Noldus) using three-point tracking. Y-maze was performed on two independent cohorts at 11 weeks ($Atrx^{+/y}$ $n = 13$; $Atrx^{R245C/y}$ $n = 13$) and 55 weeks ($Atrx^{+/y}$ $n = 9$; $Atrx^{R245C/y}$ $n = 9$). The Y-shaped arena consists of three arms of identical length at 120° angles. Mice were placed at the end of one arm (facing the end) and allowed to explore for 8 min. Behaviour was monitored and analysed using Ethovision XT 13 software (Noldus). Contextual and cued fear conditioning was performed on two independent cohorts at 13 weeks ($Atrx^{+/y}$ $n = 14$; $Atrx^{R245C/y}$ $n = 13$) and 56 weeks ($Atrx^{+/y}$ $n = 13$; $Atrx^{R245C/y}$ $n = 13$). On day 1, animals were placed in the testing chamber for 5 min and subjected to a 30 s tone (85 dB) ending in a 2 s, 0.75 mA foot shock (programme: 120 s baseline, 30 s tone ending in 2 s foot shock, 150 s no stimuli). On day 2 (morning), contextual fear memory was assessed by returning animals to the same testing chamber for 5 min (programme: 300 s no stimuli); and (afternoon) cued fear memory was assessed by returning animals to a testing chamber that appeared different (by adding a black triangular insert and white floor wiped with acetic acid) and playing them the same tone for 3 min (programme: 120 s baseline, 180 s tone). Behaviour was monitored and analysed using VideoFreeze™ Fear Conditioning software (Med Associates Inc).

Quantification and statistical analysis

Analysis of patient mutations

The list of unique ATR-X syndrome patient mutations and their frequency (number of cases) were obtained from (19).

Quantification of western blots

Densitometry analysis was performed using ImageJ. Genotypes were compared using *t*-tests (unpaired, two-tailed).

Quantification of immunofluorescence

Cell counts were performed on three to five sections per animal and a minimum of 3 mice per genotype were used. Counts were expressed as a percentage of total DAPI+ cells unless stated otherwise. Coronal sections from control and mutant animals were first matched using age appropriate and specific brain landmarks located outside of the cortex. Following immunostaining, an identical sized box was oriented over the dorsomedial region of the telencephalon within which DAPI+ and marker+ cells were counted for all genotypes. For Purkinje cell counts, absolute numbers of calbindin+ cells were quantified across cerebellar lobes I–VII using Image J to quantify the distance of the Purkinje cell layer. Cell number was then presented as the average number of calbindin+ cells per 100 μm. The thickness of the corpus callosum was assessed rostrally (Bregma 0.86), medially (Bregma 0.5) and caudally (Bregma 0.26) by averaging three measurements per location. Genotypes were compared using *t*-tests (unpaired, two-tailed).

Analysis of alpha globin loci

Dot plots show sequence identity within the human and mouse alpha-globin loci and were generated using the Pustell DNA Matrix method in MacVector version 13.0.7 using the following parameters: Scoring matrix: DNA identity; Window size: 30; Hash value: 8; Minimum similarity: 60%.

Analysis of MRI data

After MRI, all images were corrected for geometric distortion (46). Registration for image alignment was then performed using the Pydpiper toolkit (50), generating a consensus average across all mice in the data set. Individual volumes were segmented by mapping onto a mouse brain atlas with 183 individual segmented structures (51–54) an automatically generated template approach (55). Volumetric comparisons were then made using multiple *t*-tests as implemented in the R statistical computing package. Statistical significance was assessed after correction for multiple comparisons using the false discovery rate (Benjamini and Hochberg procedure). Cortical thickness was computed at each point on the outer surface of the cerebral cortex using the method described in (56). Briefly, this method defines the inner and outer cortical surface as electrostatic potentials and solves for the length of field lines connecting the two surfaces.

Additional MRI data were obtained from (10) for comparison with *Atrx*$^{fl/y}$*; CaMKIICre* (*CaMKII-cKO*) mice.

Sholl analysis

Cultured Hippocampal neurons were stained for MAP2 (1:1000, AB5622 Merck Millipore) and Tau-1 (1:1000 MAB3420, Merk millipore) to distinguish dendrites and axons, respectively, and counterstained with Hoescht 33342 dye (Thermo Fisher Scientific). z-stack images were obtained using Zeiss AxioObserver Z1 and later processed using SNT plugins on FIJI to obtain a traced 2D binary representation of the dendrites for Sholl analysis using 10 μm steps and the number of crossings were counted until a radius of 150 μm. Genotypes were compared using Mixed-Effects analysis. We also evaluated the total length and axonal length and genotypes were compared using KS tests.

Statistical analysis of morphological and behavioural data

Growth curves were compared using repeated measures ANOVA. DEXA, Brain weights, TA muscle weights and TA/body weights were compared using *t*-tests (unpaired, two-tailed).

X-ray images were measured using MicroDicom software. Body length was measured from nose to base of tail and genotypes were compared using a *t*-test (unpaired, two-tailed). Cranial index (%) = (cranial width/cranial length × 100). Zygomatic index (%) = (zygomatic width/zygomatic length × 100), where zygomatic length is the mean of the left and right measurements. Kyphotic index = AB/CD, where AB is the length of a line drawn from posterior edge of C7 to the posterior edge of L6 and CD is the distance from line AB to the dorsal border of the vertebral body farthest from that line (drawn perpendicular to line AB) (57). When data fit a normal distribution (cranial length, cranial index at 40 weeks, zygomatic length, zygomatic index and kyphotic index), genotypes were compared using *t*-tests (unpaired, two-tailed). Otherwise (cranial index at 14 weeks), genotypes were compared using KS tests.

The mean of three grip strength recordings (gram-force, GF) was normalized by body weight and genotypes were compared using *t*-tests (unpaired, two-tailed). Gait analysis parameters were exported from DigiGait Analysis 15 software and genotypes were compared using *t*-tests (if normally distributed) or KS tests. Stride length, analysed by *t*-tests (unpaired, two-tailed) and stance width coefficient of variation (Cv), analysed by a KS test (unpaired, two-tailed) at 10 weeks and a *t*-test at 55 weeks are shown. Treadmill performance during trials (days 5–7) was compared for each day using Mann–Whitney tests. Feret's diameter from TA muscle after chronic exercise was compared using repeated measures ANOVA.

Spontaneous locomotor activity in SHIRPA was compared using *t*-tests (unpaired, two-tailed). In the Open Field assay, distance travelled was assessed in four 5 min bins and genotypes were compared using repeated measures ANOVA. For each bin, genotypes were compared using *t*-tests (unpaired, two-tailed). In the Open Field assay, time spent in the central 40% of the arena was assessed in four 5 min bins and genotypes were compared using repeated measures ANOVA. In the Light/Dark test, time spent in the light half was assessed in three 5 min bins and genotypes were compared using repeated measures ANOVA. In the Elevated Zero Maze, time spent in the open quadrants was compared using a *t*-test (unpaired, two-tailed).

Baseline motor function was assessed by accelerating rotarod performance (latency to fall) during four trails on day 1. At 13 weeks, the data fit a normal distribution and so genotypes were compared using repeated measures ANOVA and improvement over the course of the day was assessed for each genotype using 1-way ANOVA. At 55 weeks, the data do not fit a normal distribution and so genotypes were compared for each trial using KS tests and improvement over the course of the day was assessed for each genotype using Friedman tests. Motor learning ability was assessed over a total of 3 days. Daily performance for each animal was determined by the mean performance (latency to fall) in the four trials for each day. At 13 weeks, the data do not fit a normal distribution and so genotypes were compared for each day using KS tests and motor learning over the course of the experiment was assessed for each genotype using Friedman tests. At 55 weeks, the data fit a normal distribution and so genotypes were compared for each day using *t*-tests and motor learning over the course of the experiment was assessed for each genotype using one-way ANOVA. Spatial learning was assessed in the Barnes maze by the time taken for the mouse to locate the escape hole, defined by its nose entering a zone around the hole. A maximum score of 180 s was assigned to animals that failed to locate the hole during the trial. Daily performance for each animal was determined by the mean time in the four trials for each day (days 2–5). Genotypes were compared on each day using KS tests. Social novelty preference was assessed by the amount of time the subject spends interacting with stranger mice (i.e. its nose is located in the sniffing zone around the cup containing the stranger mouse). Time spent sniffing stranger 1 versus 2 was assessed for each genotype using *t*-tests (paired, two-tailed). Spatial reference memory was assessed over 8 min in the Y-maze test. Alternation index = number of alternations/max alternations × 100. Genotypes were compared using *t*-tests (unpaired, two-tailed). Fear memory was determined by the time spent freezing (minus the baseline) the day after being subjected to foot shock, in response to being returned to the same chamber (contextual) or hearing the same tone (cued). In the contextual paradigm, time spent freezing was assessed in 1 min bins over the 5 min trial (minus baseline determined on day 1 prior to stimuli). Genotypes were compared using repeated measures ANOVA. In the cued paradigm, time spent freezing was assessed during the 3 min tone (minus baseline determined in the same trial prior to the tone). At 13 weeks, the data do not fit a normal distribution and so genotypes were compared using a KS test. At 56 weeks, the data fit a normal distribution and so genotypes were compared using a *t*-test (unpaired, two-tailed).

All statistical analysis of morphological and behavioural data was performed using GraphPad Prism 9. Significance thresholds:

not significant (NS) $P > 0.05$; *$P < 0.05$; **$P < 0.01$; ***$P < 0.001$; ****$P < 0.0001$.

Supplementary Material

Supplementary material is available at *HMG* online.

Acknowledgements

The authors wish to acknowledge the contribution of Lauryl Nutter and Marina Gertsenstein in the TCP Model Production Core for the generation of the *Atrx*^{em1Tcp} mutant mice; and Ann Flenniken and Zorana Berberovic in the TCP Clinical Phenotyping Core for X-ray imaging, DEXA and blood analysis. We thank Igor Vukobradovic, Gabi Gurria, Sebastian Gerety and Matthew Hurles for advice on behavioural testing and analysis of craniofacial morphology; Eleonora Maino for advice on muscle analysis; and Tiffany Chien, Ron Padilla and Zachary Klugman for technical assistance. We also thank members of the Justice, Picketts, R.J. Gibbons and D.R. Higgs laboratories for helpful discussions.

Conflict of Interest statement. None declared.

Funding

Sir Henry Wellcome Postdoctoral Fellowship (210913/Z/18/Z to R.T.); Canadian Institutes of Health Research (FDN-15423 to M.J.J. and MOP133586; MOP142398 to D.J.P.).

Data Availability

The MRI image data are available upon reasonable request.

References

1. Gibbons, R.J., Picketts, D.J., Villard, L. and Higgs, D.R. (1995) Mutations in a putative global transcriptional regulator cause X-linked mental retardation with α-thalassemia (ATR-X syndrome). *Cell*, **80**, 837–845.
2. Timpano, S. and Picketts, D.J. (2020) Neurodevelopmental disorders caused by defective chromatin Remodeling: phenotypic complexity is highlighted by a review of ATRX function. *Front. Genet.*, **11**, 885.
3. Heaphy, C.M., de Wilde, R.F., Jiao, Y., Klein, A.P., Edil, B.H., Shi, C., Bettegowda, C., Rodriguez, F.J., Eberhart, C.G., Hebbar, S. *et al.* (2011) Altered telomeres in tumors with ATRX and DAXX mutations. Altered telomeres in tumors with ATRX and DAXX mutations. *Science*, **333**, 425.
4. Kent, T. and Clynes, D. (2021) Alternative lengthening of telomeres: lessons to be learned from Telomeric DNA double-strand break repair. *Genes (Basel)*, **12**, 1734.
5. Stevenson, R.E. (2020) Alpha-Thalassemia X-Linked Intellectual Disability Syndrome. In *GeneReviews® [Internet]*. University of Washington, Seattle, Seattle, WA 1993–2020.
6. Gibbons, R.J. (2012) α-Thalassemia, mental retardation, and myelodysplastic syndrome. *Cold Spring Harb. Perspect. Med.*, **2**, a011759.
7. Garrick, D., Sharpe, J.A., Arkell, R., Dobbie, L., Smith, A.J.H., Wood, W.G., Higgs, D.R. and Gibbons, R.J. (2006) Loss of Atrx affects trophoblast development and the pattern of X-inactivation in extraembryonic tissues. *PLoS Genet.*, **2**, 438–450.
8. Bérubé, N.G., Mangelsdorf, M., Jagla, M., Vanderluit, J., Garrick, D., Gibbons, R.J., Higgs, D.R., Slack, R.S. and Picketts, D.J. (2005) The chromatin-remodeling protein ATRX is critical for neuronal survival during corticogenesis. *J. Clin. Investig.*, **115**, 258–267.
9. Tamming, R.J., Siu, J.R., Jiang, Y., Prado, M.A.M., Beier, F. and Bérubé, N.G. (2017) Mosaic expression of *Atrx* in the mouse central nervous system causes memory deficits. *Dis. Model. Mech.*, **10**, 119–126.
10. Tamming, R.J., Dumeaux, V., Jiang, Y., Shafiq, S., Langlois, L., Ellegood, J., Qiu, L.R., Lerch, J.P. and Bérubé, N.G. (2020) Atrx deletion in neurons leads to sexually dimorphic dysregulation of miR-137 and spatial learning and memory deficits. *Cell Rep.*, **31**, 107838.
11. Medina, C.F., Mazerolle, C., Wang, Y., Bérubé, N.G., Coupland, S., Gibbons, R.J., Wallace, V.A. and Picketts, D.J. (2009) Altered visual function and interneuron survival in Atrx knockout mice: inference for the human syndrome. *Hum. Mol. Genet.*, **18**, 966–977.
12. Lagali, P.S., Medina, C.F., Zhao, B.Y.H., Yan, K., Baker, A.N., Coupland, S.G., Tsilfidis, C., Wallace, V.A. and Picketts, D.J. (2016) Retinal interneuron survival requires non-cell-autonomous Atrx activity. *Hum. Mol. Genet.*, **25**, 4787–4803.
13. Solomon, L.A., Li, J.R., Bérubé, N.G. and Beier, F. (2009) Loss of ATRX in chondrocytes has minimal effects on skeletal development. *PLoS One*, **4**, e7106.
14. Huh, M.S., O'Dea, T.P., Ouazia, D., McKay, B.C., Parise, G., Parks, R.J., Rudnicki, M.A. and Picketts, D.J. (2012) Compromised genomic integrity impedes muscle growth after Atrx inactivation. *J. Clin. Investig.*, **122**, 4412–4423.
15. Huh, M.S., Young, K.G., Yan, K., Price-O'Dea, T. and Picketts, D.J. (2017) Recovery from impaired muscle growth arises from prolonged postnatal accretion of myonuclei in Atrx mutant mice. *PLoS One*, **12**, e0186989.
16. Bagheri-fam, S., Argentaro, A., Svingen, T., Combes, A.N., Sinclair, A.H., Koopman, P. and Harley, V.R. (2011) Defective survival of proliferating sertoli cells and androgen receptor function in a mouse model of the ATR-X syndrome. *Hum. Mol. Genet.*, **20**, 2213–2224.
17. Muers, M.R., Sharpe, J.A., Garrick, D., Sloane-Stanley, J., Nolan, P.M., Hacker, T., Wood, W.G., Higgs, D.R. and Gibbons, R.J. (2007) Defining the cause of skewed X-chromosome inactivation in X-linked mental retardation by use of a mouse model. *Am. J. Hum. Genet.*, **80**, 1138–1149.
18. Howard, M.T., Malik, N., Anderson, C.B., Voskuil, J.L.A., Atkins, J.F. and Gibbons, R.J. (2004) Attenuation of an amino-terminal premature stop codon mutation in the ATRX gene by an alternative mode of translational initiation. *J. Med. Genet.*, **41**, 951–956.
19. Gibbons, R.J., Wada, T., Fisher, C.A., Malik, N., Mitson, M.J., Steensma, D.P., Fryer, A., Goudie, D.R., Krantz, I.D. and Traeger-Synodinos, J. (2008) Mutations in the chromatin-associated protein ATRX. *Hum. Mutat.*, **29**, 796–802.
20. Gibbons, R.J. and Higgs, D.R. (2000) Molecular—clinical spectrum of the ATR-X syndrome. *Am. J. Med. Genet.*, **97**, 204–212.
21. Argentaro, A., Yang, J.C., Chapman, L., Kowalczyk, M.S., Gibbons, R.J., Higgs, D.R., Neuhaus, D. and Rhodes, D. (2007) Structural consequences of disease-causing mutations in the ATRX-DNMT3-DNMT3L (ADD) domain of the chromatin-associated protein ATRX. *Proc. Natl. Acad. Sci.*, **104**, 11939–11944.
22. Mitson, M., Kelley, L.A., Sternberg, M.J.E., Higgs, D.R. and Gibbons, R.J. (2011) Functional significance of mutations in the Snf2 domain of ATRX. *Hum. Mol. Genet.*, **20**, 2603–2610.
23. Iwase, S., Xiang, B., Ghosh, S., Ren, T., Lewis, P.W., Cochrane, J.C., Allis, C.D., Picketts, D.J., Patel, D.J., Li, H. *et al.* (2011) ATRX ADD domain links an atypical histone methylation recognition mechanism to human mental-retardation syndrome. *Nat. Struct. Mol. Biol.*, **18**, 769–776.

24. Nogami, T., Beppu, H., Tokoro, T., Moriguchi, S., Shioda, N., Fukunaga, K., Ohtsuka, T., Ishii, Y., Sasahara, M., Shimada, Y. *et al.* (2011) Reduced expression of the ATRX gene, a chromatin-remodeling factor, causes hippocampal dysfunction in mice. *Hippocampus*, **21**, 678–687.
25. Shioda, N., Beppu, H., Fukuda, T., Li, E., Kitajima, I. and Fukunaga, K. (2011) Aberrant calcium/Calmodulin-dependent protein kinase II (CaMKII) activity is associated with abnormal dendritic spine morphology in the ATRX mutant mouse brain. *J. Neurosci.*, **31**, 346–358.
26. Seah, C., Levy, M.A., Jiang, Y., Mokhtarzada, S., Higgs, D.R., Gibbons, R.J. and Berube, N.G. (2008) Neuronal death resulting from targeted disruption of the Snf2 protein ATRX is mediated by p53. *J. Neurosci.*, **28**, 12570–12580.
27. Gibbons, R. (2006) Alpha thalassaemia-mental retardation, X linked. *Orphanet. J. Rare. Dis.*, **1**, 15. https://ojrd.biomedcentral.com/articles/10.1186/1750-1172-1-15.
28. Vaisfeld, A., Taormina, S., Simonati, A. and Neri, G. (2022) Phenotypic Spectrum and molecular findings in 17 ATR-X syndrome Italian patients: some new insights. *Genes (Basel)*, **13**, 1792.
29. Law, M.J., Lower, K.M., Voon, H.P.J., Hughes, J.R., Garrick, D., Viprakasit, V., Mitson, M., de Gobbi, M., Marra, M., Morris, A. *et al.* (2010) ATR-X syndrome protein targets tandem repeats and influences allele-specific expression in a size-dependent manner. *Cell*, **143**, 367–378.
30. Huh, M.S., Ivanochko, D., Hashem, L.E., Curtin, M., Delorme, M., Goodall, E., Yan, K. and Picketts, D.J. (2016) Stalled replication forks within heterochromatin require ATRX for protection. *Cell Death Dis.*, **7**, e2220.
31. Wada, T., Ban, H., Matsufuji, M., Okamoto, N., Enomoto, K., Kurosawa, K. and Aida, N. (2013) Neuroradiologic features in α-linked α-thalassemia/mental retardation syndrome. *Am. J. Neuroradiol.*, **34**, 2034–2038.
32. Lee, J.S., Lee, S., Lim, B.C., Kim, K.J., Hwang, Y.S., Choi, M. and Chae, J.H. (2015) Alpha-thalassemia X-linked intellectual disability syndrome identified by whole exome sequencing in two boys with white matter changes and developmental retardation. *Gene*, **569**, 318–322.
33. Thienpont, B., de Ravel, T., van Esch, H., van Schoubroeck, D., Moerman, P., Vermeesch, J.R., Fryns, J.P., Froyen, G., Lacoste, C., Badens, C. *et al.* (2007) Partial duplications of the ATRX gene cause the ATR-X syndrome. *Eur. J. Hum. Genet.*, **15**, 1094–1097.
34. Leto, K., Arancillo, M., Becker, E.B.E., Buffo, A., Chiang, C., Ding, B., Dobyns, W.B., Dusart, I., Haldipur, P., Hatten, M.E. *et al.* (2016) Consensus paper: cerebellar development. Consensus paper: cerebellar development. *Cerebellum*, **15**, 789–828.
35. Abidi, F.E., Cardoso, C., Lossi, A.-M., Lowry, R.B., Depetris, D., Mattéi, M.-G., Lubs, H.A., Stevenson, R.E., Fontes, M., Chudley, A.E. *et al.* (2005) Mutation in the 5' alternatively spliced region of the XNP/ATR-X gene causes Chudley-Lowry syndrome. *Eur. J. Hum. Genet.*, **13**, 176–183.
36. Bérubé, N.G., Jagla, M., Smeenk, C., de Repentigny, Y., Kothary, R. and Picketts, D.J. (2002) Neurodevelopmental defects resulting from ATRX overexpression in transgenic mice. *Hum. Mol. Genet.*, **11**, 253–261.
37. Fukada, S.I., Morikawa, D., Yamamoto, Y., Yoshida, T., Sumie, N., Yamaguchi, M., Ito, T., Miyagoe-Suzuki, Y., Takeda, S., Tsujikawa, K. *et al.* (2010) Genetic background affects properties of satellite cells and mdx phenotypes. *Am. J. Pathol.*, **176**, 2414–2424.
38. Wong, T.W.Y., Ahmed, A., Yang, G., Maino, E., Steiman, S., Hyatt, E., Chan, P., Lindsay, K., Wong, N., Golebiowski, D. *et al.* (2020) A novel mouse model of Duchenne muscular dystrophy carrying a multi-exonic DMD deletion exhibits progressive muscular dystrophy and early-onset cardiomyopathy. *Dis. Model. Mech.*, **13**.
39. Truch, J., Downes, D.J., Scott, C., Gür, E.R., Telenius, J.M., Repapi, E., Schwessinger, R., Gosden, M., Brown, J.M., Taylor, S. *et al.* (2022) The chromatin remodeller ATRX facilitates diverse nuclear processes, in a stochastic manner, in both heterochromatin and euchromatin. *Nat. Commun.*, **13**, 3485.
40. Bieluszewska, A., Wulfridge, P., Doherty, J., Ren, W. and Sarma, K. (2022) ATRX histone binding and helicase activities have distinct roles in neuronal differentiation. *Nucleic Acids Res.*, **50**, 9162–9174.
41. Watson, L.A., Solomon, L.A., Li, J.R., Jiang, Y., Edwards, M., Shin-Ya, K., Beier, F. and Bérubé, N.G. (2013) Atrx deficiency induces telomere dysfunction, endocrine defects, and reduced life span. *J. Clin. Investig.*, **123**, 2049–2063.
42. Dyer, M.A., Qadeer, Z.A., Valle-Garcia, D. and Bernstein, E. (2017) ATRX and DAXX: mechanisms and mutations. *Cold Spring Harb. Perspect. Med.*, **7**, a026567.
43. Gertsenstein, M. and Nutter, L.M.J. (2021) Production of knockout mouse lines with Cas9. *Methods*, **191**, 32–43.
44. Wilson, C., Rozés-Salvador, V. and Cáceres, A. (2020) Protocol for evaluating neuronal polarity in murine models. *STAR Protoc.*, **1**, 100114.
45. McDowell, T.L., Gibbons, R.J., Sutherland, H., O'Rourke, D.M., Bickmore, W.A., Pombo, A., Turley, H., Gatter, K., Picketts, D.J., Buckle, V.J. *et al.* (1999) Localization of a putative transcriptional regulator (ATRX) at pericentromeric heterochromatin and the short arms of acrocentric chromosomes. *Proc. Natl. Acad. Sci.*, **96**, 13983–13988.
46. Nieman, B.J., van Eede, M.C., Spring, S., Dazai, J., Henkelman, R.M. and Lerch, J.P. (2018) MRI to assess neurological function. *Curr. Protoc. Mouse Biol.*, **8**, e44.
47. Arbabi, A., Spencer Noakes, L., Vousden, D., Dazai, J., Spring, S., Botelho, O., Keshavarzian, T., Mattingly, M., Ellegood, J.E., Nutter, L.M.J. *et al.* (2022) Multiple-mouse magnetic resonance imaging with cryogenic radiofrequency probes for evaluation of brain development. *NeuroImage*, **252**, 119008.
48. Nieman, B.J., Szulc, K.U. and Turnbull, D.H. (2009) Three-dimensional, in vivo MRI with self-gating and image coregistration in the mouse. *Magn. Reason. Med.*, **61**, 1148–1157.
49. Spencer Noakes, T.L., Henkelman, R.M. and Nieman, B.J. (2017) Partitioning k-space for cylindrical three-dimensional rapid acquisition with relaxation enhancement imaging in the mouse brain. *NMR Biomed.*, **30**, e3802.
50. Friedel, M., van Eede, M.C., Pipitone, J., Mallar Chakravarty, M. and Lerch, J.P. (2014) Pydpiper: a flexible toolkit for constructing novel registration pipelines. *Front. Neuroinform.*, **8**, 67.
51. Dorr, A.E., Lerch, J.P., Spring, S., Kabani, N. and Henkelman, R.M. (2008) High resolution three-dimensional brain atlas using an average magnetic resonance image of 40 adult C57Bl/6J mice. *NeuroImage*, **42**, 60–69.
52. Ullmann, J.F.P., Watson, C., Janke, A.L., Kurniawan, N.D. and Reutens, D.C. (2013) A segmentation protocol and MRI atlas of the C57BL/6J mouse neocortex. *NeuroImage*, **78**, 196–203.
53. Steadman, P.E., Ellegood, J., Szulc, K.U., Turnbull, D.H., Joyner, A.L., Henkelman, R.M. and Lerch, J.P. (2014) Genetic effects on cerebellar structure across mouse models of autism using a magnetic resonance imaging atlas. *Autism Res.*, **7**, 124–137.
54. Richards, K., Watson, C., Buckley, R.F., Kurniawan, N.D., Yang, Z., Keller, M.D., Beare, R., Bartlett, P.F., Egan, G.F., Galloway, G.J. *et al.* (2011) Segmentation of the mouse hippocampal formation in magnetic resonance images. *NeuroImage*, **58**, 732–740.
55. Chakravarty, M.M., Steadman, P., van Eede, M.C., Calcott, R.D., Gu, V., Shaw, P., Raznahan, A., Collins, D.L. and Lerch, J.P.

(2013) Performing label-fusion-based segmentation using multiple automatically generated templates. *Hum. Brain Mapp.*, **34**, 2635–2654.

56. Lerch, J.P., Carroll, J.B., Dorr, A., Spring, S., Evans, A.C., Hayden, M.R., Sled, J.G. and Henkelman, R.M. (2008) Cortical thickness measured from MRI in the YAC128 mouse model of Huntington's disease. *NeuroImage*, **41**, 243–251.
57. Laws, N. and Hoey, A. (2004) Progression of kyphosis in mdx mice. *J. Appl. Physiol.*, **97**, 1970–1977.